




Review

Recent Advances in MXene-Based Nanocomposites for Wastewater Purification and Water Treatment: A Review

Zahra Pouramini ¹, Seyyed Mojtaba Mousavi ^{2,*}, Aziz Babapoor ³, Seyyed Alireza Hashemi ⁴ , Nelson Pynadathu Rumjit ⁵, Shivani Garg ⁶, Shakeel Ahmed ^{7,8,9}  and Wei-Hung Chiang ^{2,*} 

¹ Department of Civil and Environmental Engineering, Tarbiat Modares University, Tehran 14115-111, Iran; pouramini.z@yahoo.com

² Department of Chemical Engineering, National Taiwan University of Science and Technology, Taipei 106, Taiwan

³ Department of Chemical Engineering, University of Mohaghegh Ardabili (UMA), Ardabil 179, Iran; babapoor@uma.ac.ir

⁴ Nanomaterials and Polymer Nanocomposites Laboratory, School of Engineering, University of British Columbia, Kelowna, BC V1V 1V7, Canada; sa_hashemi@sums.ac.ir

⁵ Nanotechnology & Catalysis Research Center (NANOCAT), Institute for Advanced Studies, University of Malaya, Kuala Lumpur 50603, Malaysia; nelsonpynadath@gmail.com

⁶ Institute of Environmental Studies, Kurukshetra University, Kurukshetra 136119, India; shivanigarg397@gmail.com

⁷ Department of Chemistry, Government Degree College Mendhar, Jammu and Kashmir 185211, India; shakeelchem11@gmail.com

⁸ Higher Education Department, Government of Jammu and Kashmir, Jammu 180001, India

⁹ University Centre for Research and Development (UCRD), Chandigarh University, Mohali 140413, India

* Correspondence: mousavi.nano@gmail.com (S.M.M.); whchiang@mail.ntust.edu.tw (W.-H.C.)

Abstract: The increase in pollutants such as hazardous refractory contaminants, organic dyes, pharmaceuticals, and pesticides entering water resources on a large scale due to global population growth and industrialization has become a significant health concern worldwide. The two-dimensional (2D) MXene material is a new type of transition metal carbide or carbonitride material, which has demonstrated the capability to adsorb various heavy contaminants, particularly metals such as chromium, copper, lead, and mercury. In addition, MXenes have a tunable band gap (0.92–1.75 eV) and exhibit good thermal stability and considerable damage resistance, which means that they are well suited as adsorbents for waste removal. In this review article, MXene nanocomposites are introduced for the removal of pollutants from water. The idea of water remediation, the applications of MXene-based nanocomposites, and the effects on the degradation of water and wastewater contaminants are reviewed. Future trends in MXene-based nanocomposites for water treatment and environmental applications will also be discussed.

Keywords: environmental; wastewater; MXene; nanocomposites



Citation: Pouramini, Z.; Mousavi, S.M.; Babapoor, A.; Hashemi, S.A.; Pynadathu Rumjit, N.; Garg, S.; Ahmed, S.; Chiang, W.-H. Recent Advances in MXene-Based Nanocomposites for Wastewater Purification and Water Treatment: A Review. *Water* **2023**, *15*, 1267. <https://doi.org/10.3390/w15071267>

Academic Editor: William Frederick Ritter

Received: 18 February 2023

Revised: 18 March 2023

Accepted: 21 March 2023

Published: 23 March 2023



Copyright: © 2023 by the authors. Licensee MDPI, Basel, Switzerland. This article is an open access article distributed under the terms and conditions of the Creative Commons Attribution (CC BY) license (<https://creativecommons.org/licenses/by/4.0/>).

1. Introduction

Social economies continue to develop, which results in an escalating need for water. However, there is a great deal of water on this planet that cannot be utilized straightaway, resulting in an enormous contradiction between the demands of people for water and the available water resources [1–4]. Researchers must find novel ways to rationally increase the water resources used in order to solve these kinds of problems. Different processing techniques have been discovered for water remediation, including splitting of water, effluent purification, and antibacterial purification of seawater. A milestone in the research and progress of water treatment equipment has been photocatalytic technology and adsorption, both of which have unique properties [5–11].

Several advanced 2D nanomaterials for environmental remediation were discussed. Despite their advantages, they had several disadvantages, including high cost, low retention capacity, and poor chemical and thermal stability. To overcome the drawbacks of conventional 2D nanomaterials, scientists have shown interest in two-dimensional substances containing nitrides and transition metal carbides, referred to as MXenes, with the chemical formula $M_{n+1}X_nT_X$ [12,13]. Due to their chemical, physical, and functional properties, MXenes are suitable for a wide range of industrial applications [14]. Early transition metal carbides and nitrides are known as important compound groups due to their high metallic electrical conductivity, high hardness, and excellent chemical stability [15]. In high-temperature applications and cutting tools, they have been investigated as bulk ceramic materials for decades. Other applications include functional composites and catalysts and electrochemical energy storage [16]. Due to the strong bonds between transition metals and carbon/nitrogen atoms (mostly covalent/metallic bonds), it is challenging to reduce their dimensionality from solid 3D solids to nanomaterials, including 2D sheets and 1D nanoribbons or nanotubes [17].

The first discovery of MXene was made by Yury Gogotsi and Michel W. Barsoum in 2011. As Ti_3AlC_2 is immersed in hydrofluoric acid (HF), it is possible to selectively remove the aluminum layer to obtain 2D titanium carbide Ti_3C_2 nanosheets with outstanding universal properties. As a result, the family of “MXenes” is utilized in order to determine the correlation between the MAX phases and their dimensions. MXenes typically have a thickness between 1 nm and 2 nm related to the n in MXenes ($M_{n+1}X_nT_X$). MXenes are mostly derived by selectively etching the A layers from the precursor MAX phase ($M_{n+1}AX_n$), in which M indicates a transition metal, A represents any element from groups 12–16 (including Cd, Al, Si, P, S, Ga, Ge, As, In, Sn, Tl, and Pb), X demonstrate C and/or N, and n indicates 1, 2, or 3 [18,19]. MX phases typically have A layers sandwiched between octahedral $M_{n+1}X_n$ structures, with relatively powerful M–X bonds and a weak bond of M–A [20]. Approximately 30 MXene compositions have been reported in the studies that were prepared from the MAX phase precursors, mostly by adding transition metals to the M layers [21]. There are several types of MXenes, but Ti-based MXenes (such as $Ti_3C_2T_X$ and Ti_2CT_X) are most widely used in environmental applications [21,22]. As a result of their special layered structure and two-dimensional morphology, MXenes can be mixed with other substances to improve their features. This particular chemical construction gives MXenes excellent electrical conductivity, flexibility, and tunable properties. In the context of environmental purification and energy production, MXenes have enticed a lot of consideration [23], including the photocatalytic oxidation of organic contaminants [24,25], heavy metals adsorption [26], sensing and catalysis [27], and fueling production and energy storage [28,29]. Currently, MXene materials are relatively new, and developing them into commercially viable products will take a lot of effort. The performance and applications of these devices are being studied by more and more researchers. According to the literature review, MXenes are most frequently discussed in the context of energy conversion [30], biomedical, and storage studies [31], and there are fewer studies on environmental cleaning and wastewater treatment (Figure 1). MXenes and MXene-based composites are examined in this review for their application in the removal of unwanted contaminants from water, with particular emphasis on dyes and heavy metals. The synthesis methods, the removal mechanism, the structure of MXenes and their role in the removal process, and the regeneration of MXenes are considered and evaluated. In addition, the current difficulties and future prospects of these great substances in wastewater and water treatment are discussed.

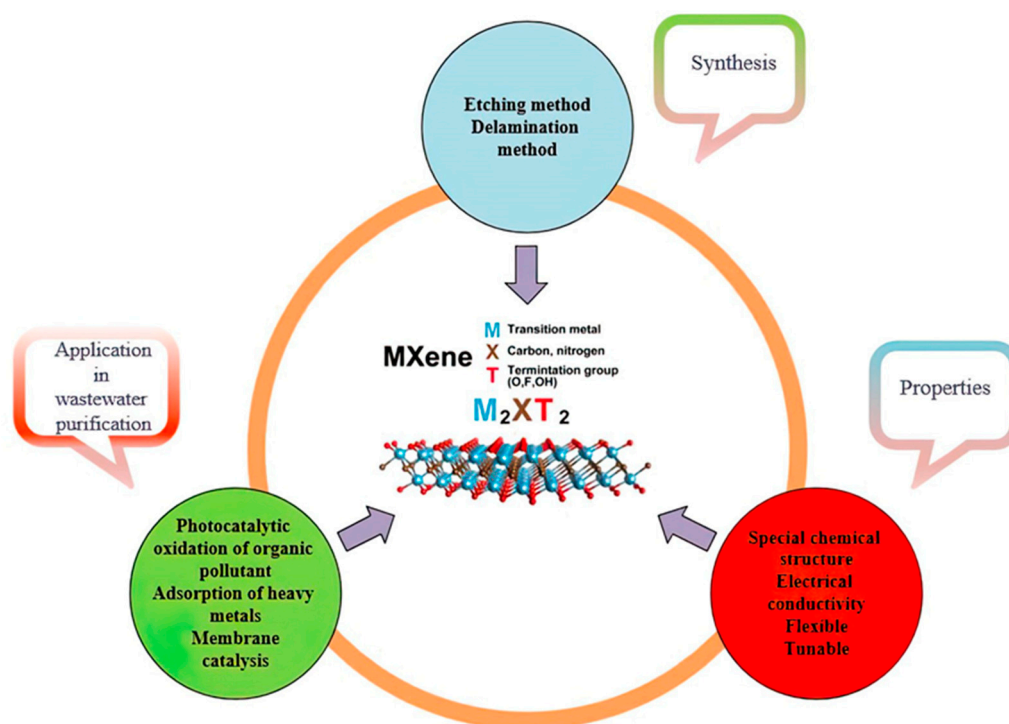


Figure 1. A description of MXene synthesis, features, and applications.

2. MXene and Nanocomposite-Based MXene Synthesis

Currently, MXenes are primarily produced through high-temperature sintering and ball milling of MAX precursors. For layer hexagonal MAX phases with two formula units per unit cell, layer M and the X-atom are strongly coupled through metallic, ionic, and covalent bonds, and the A-atom layers penetrate among layers of $M_{n+1}X_n$. They are connected with the M atom via perfect metallic bonds [32–34]. The force among A and M in the MAX phase unit cell seems weaker than the force among M and X, which is more susceptible to damage [35]. The metallic bonds among elements of A and M are difficult to break through mechanical exfoliation, unlike in the other lamellar substances connected with van der Waals forces [36]. Fortunately, it was demonstrated that even when purified via acid and ultrasonic conditions, the bonds of M–A were simply broken, but the M–X bonds did not break completely [37]. It is, therefore, common to obtain MXene by selectively etching A-phase from MAX.

2.1. Etching Approach

For the preparation of MXene, two primary etching methods are used; HF and in situ HF [38]. Since high risks are associated with the critical corrosiveness of HF, utilization of a high concentration of HF was avoided, and the in situ HF method was invented [39]. Other reagents, such as NaOH and H_2SO_4 , can also be used to etch the A layers without F^- [40]. In the preparation procedure, the primary etching purpose is the adequate exfoliating of A layers from the MAX phases [32]. Etchant concentration and type remain critical factors in the process. For wet chemical etching to be successful, it is necessary to have convenient etchants and synthesis conditions. Depending on their properties, the etched matter differs [32,38,41,42]; despite the lack of sufficient research, [38] referred that they applied the HF solution concentrated at 50%. On the contrary, by using wet etching techniques, other types of multilayer MXene have been synthesized with various MAX phase elements. During the layering step, intercalation is used to produce monolayer MXenes by the addition of massive organic substances within the layers, including C_2H_6OS , $NH_2NH_2 \cdot H_2O$, CH_4N_2O , $C_{16}H_{37}NO$, and C_3H_9N [43–45]. The result will be the same regardless of ammonium bifluoride and HCl or HF [46]. There is an alternative method

for etching the A layer. NaOH and H₂SO₄ can be used instead of fluorine-containing etchants [40]. In the delamination section, the kind and concentration of the etchant process show an influential role in the subsequent process and MXene preparation.

2.1.1. HF Approach

The etching of HF is performed by soaking the MAX phase in a solution containing hydrofluoric acid, which is a commonly used etchant for etching Al, Si, C, and N layers in group A [32,38,47]. AlF₃ is formed by reacting element A with F[−] and etching in the MAX phase. MXene's surface also contains fluorine (F), which is part of its functional group, as HF reacts with multiple layers of MXene [32]. It should be noted that the hydrofluoric acid solution concentration, the temperature, the soaking time, and the circumstances of etching could significantly influence the structure of MXenes. As a result, finding the right etching conditions to enhance the MXene's performance is challenging [41,42,45]. Etchant concentrations range from 5 to 50 wt.% hydrofluoric acid and exposure times range from 5 to 24 h according to the concentration [38,47,48].

The MXene structure was observed to be affected by changing the HF solution concentration. It is possible to produce more sophisticated Ti₃C₂T_x etching at higher HF concentrations [38]. With XRD and EDX analysis, Alhabeab et al. investigated the efficiency of the etching of 5, 10, and 30 wt.% of hydrofluoric acid solution. In this study, the hydrofluoric acid concentration etchant had an instrumental role in the exfoliating A-layers. MXene with an HF content of 30 wt.% displayed an almost accordion-like structure on SEM images. As the outcomes exhibited, the morphology of MXene in 10 wt.% and 5 wt.% hydrofluoric acid solutions had an insignificant level of openness and virtually no growth. Thus, using a high HF concentration could produce MXene with a structure with an accordion-like appearance and an increased surface area [38]. Furthermore, Chang et al. investigated Ti₃AlC₂ powders and showed that the etching procedure findings are not just influenced by the concentration of hydrofluoric acid solution but also by the length of immersion of the MAX phase in hydrofluoric acid solution, with an increase in the duration of reaction, thinned MXene layers could be observed. A weakening trend in peaks of diffraction was observed via an extensive soaking period of 4 to 20 min h in the Ti₃AlC₂ XRD patterns and the HF-treated sample. As a result of the extended reaction time, the multilayer that resulted from MXene was thinner. A hydrothermal-assisted approach was used by Wang et al. To prepare V₂CT_x MXene from etched V₂AlC using fluoride and hydrochloric acid solutions. Based on the obtained results, MXene V₂CT_x was found to have outstanding electrochemical features in lithium-ion batteries as an anode [49]. Moreover, [50] exhibited the electrochemical etching of Al from porous Ti₂AlC electrodes in dilute HF to produce a Ti₂CT_x MXene layer on Ti₂AlC. Based on the results, it is evident that the composition and etching conditions can be adjusted widely [50].

2.1.2. HF Solution

To reduce the risks involved by utilizing HF solution with high concentrations in the production of MXene, this method of etching was introduced as a safer way for production [46]. A HF etching method was used by Naguib et al. to synthesize various MXenes [51]. Finally, the MAX phase is etched into the MAX phase through the reaction between element A and fluorine in the HF solution [41]. Hydrofluoric acid or form hydrofluoric acid via the reaction is the primary reagent compound utilized during the procedure. Ammonium bifluoride and ammonium fluoride are the two frequently utilized reagents to achieve the HF process effect, which allows the MAX layers to be exfoliated [52–54]. There are several etchants that have the peculiarity of varying MXene states as a function of their concentrations, such as FeF₃/HCl [55] and LiF/HCl [42,52,56]. The research results of Ghidui et al. demonstrated that drilling of the A layers was well done, and sonication could be shortened from 4 h to 30–60 min to decrease the MXene's synthesis time. A comparison of the lattice factors of c revealed no peaks relative to Ti₃AlC₂; the parameters of MXene etched with LiF/HCl obtained 2.80 nm, and the c network of aqueous MXene produced

via LiF/HCl reached 4.0 nm. However, only 2.0 nm of MXene parameters were etched with hydrofluoric acid utilizing 5 M LiF and 6 M HCl to etch Al in Ti_3AlC_2 [52]. However, Lipatov et al. demonstrated that using LiF concentrations and HCl concentrations of more than 5 M and 6 M, respectively, can reduce the need for sonication in this approach [42], as both etching and intercalation can be conducted at the same time, and the sonication is not required in the manufacturing procedure [32,45,46].

Using thin two-dimensional Ti_3C_2 films simplifies etching. A more spacious nitrogen interlayer results from the formation of $(\text{NH}_4)_3\text{AlF}_6$, which permits the selective etching of Al according to X-ray photoelectron spectroscopy (XPS) analyses. The lattice parameter c affirmed via XRD for $\text{Ti}_3\text{C}_2\text{T}_x$ etched utilizing NH_4HF_2 is 2.40 nm. The network modulus c increased by approximately 25% compared to HF at 1.98 nm [46]. A method was developed by Lipatov et al. for preparing well-strained $\text{Ti}_3\text{C}_2\text{T}_x$ membranes, which have the greatest Young's modulus for nanoindentation tests discussed in studies [48].

2.2. Delamination Method

The delamination process involves interpolation and sonication [38]. The intercalation process involves introducing ions and molecules between the excavated layers of MXene. It expands the interlayer space among layers, enhancing the surface area and even separating layers into 2D structures [43,57]. A sonication stage is utilized if a special MXene flake concentration or volume is requested, where the partitioned MXene is sonicated for the generation of the desired flake or concentration of two-dimensional MXene [58,59].

2.2.1. Intercalation Method

In order to remove ions or organic compounds from nonlaminated MXene layers, intercalation is used before sonication [60–62]. The functional groups involving OH and eF provide the formation of the multilayer surface for MXene after HF etching. Nevertheless, intercalation increases the net selectivity of purpose contaminants because some primary functional groups are replaced by other cations from interplants [63].

It is possible that some materials, including $\text{C}_2\text{H}_6\text{OS}$ and tetra-alkyl ammonium, such as tetrahydroxide, interfere with Al and $\text{C}_4\text{H}_{13}\text{NO}$; because of the great possibility of Lip ions inserted among the layers, the etchants utilized in situ hydrofluoric acid approach such as LiF/HCl or even NH_4HF_2 can be an intercalant [38,44,64,65]. Intercalation and potential intercalations, particularly alkaline intercalants, have been the subject of extensive research [55,66]; one molecule that can act as an intercalating species is H_2O , which can expand the network parameter [52].

2.2.2. Sonication Method

The last stage in the manufacture of MXene is sonication, which allows the control of the size and concentration of flakes [67]. Centrifugation can be used to separate the bigger MXene compounds from a solution containing the little colloidal MXene particles [38,55]. However, centrifugation omitting sonication is still a restricted option; however, sonication can increase MXene colloid concentration by exfoliating undissociated particles from the solution [44]. High efficiency is achieved when higher concentrations and smaller flakes are used than MXene (Figure 2). Various MAX phases have been etched and exfoliated to produce several different kinds of MXenes, such as $\text{Ti}_3\text{C}_2\text{T}_x$ [52], V_2C [68], Nb_2CT_x [69], Nb_4C_3 [70], Ta_4AlC_3 [71], Ti_4N_3 [72], and Mo_2C [73]. The suitable environmentally friendly solvents for liquid phase exfoliation in this method are some materials such as Polar clean [74,75], Iris [76,77], and Cyrene [75]. Table 1 shows the different types of MXs synthesized with different precursors and auxiliaries.

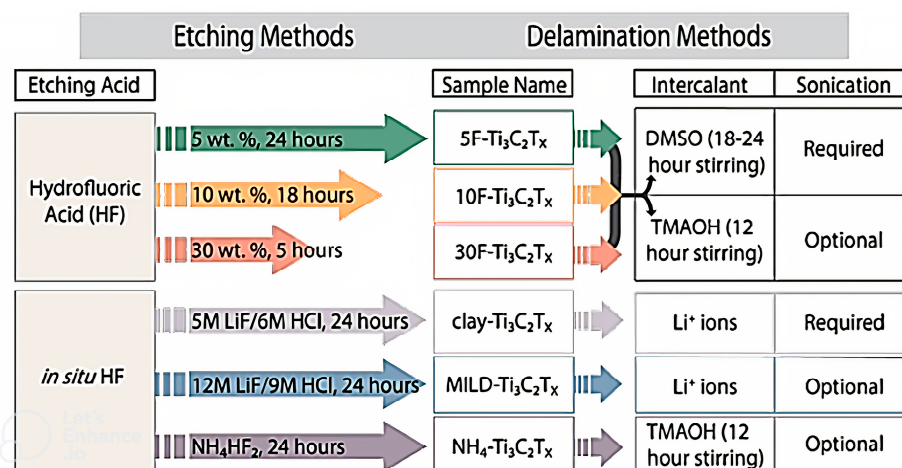


Figure 2. Synthesis of ways to produce DL-Ti₃C₂T_x by direct HF and in situ HF approach [38].

Table 1. Fabrication of different MXenes.

Kind of Precursors	Kinds of Etchants	Duration	MXene	Ref.
Ti ₃ AlC ₂	1.3 g of LiF + 6 M HCl	24 h	Ti ₃ C ₂ T _x	[78]
Cr ₂ AlC	0.2 g LiF + 2 M solution	30 min	Cr ₂ CT _x	[79]
Ti ₃ AlC ₂	NH ₃ F	24 h	Ti ₂ C ₂ T _x	[80]
Ti ₃ AlC	48% HF	30 h	Ti ₃ C ₂ T _x	[81]
Ti ₃ AlC ₂	1g MAX + 10 Ml hf	24 h	Ti ₃ C ₂ T _x	[82]

3. Features of MXenes

The characteristics of MXenes include a large Young modulus, high electric conductivities, and substantial fluctuations in band gaps [23]. In comparison to other two-dimensional materials, such as GO, MXenes have a hydrophilic texture and high metallic conductivity [38]. Modifications to their surfaces, mixtures, and morphologies can alter their features and applications [83]. By changing functional groups and developing solid solutions, the important features and electronic features of MXenes can be improved. In comparison with CNTs and reduced graphene samples, MXene is reported to have a similar electrical conductivity to that of GO nanosheets [51]. Ti₃C₂T_x exhibits a wide range of electrical conductivities depending on (1) the d-spacing of MXene flake, (2) the concentration of imperfections, (3) lateral sizes prepared by the different etching techniques, (4) external functional groups, and (5) yield of delaminations. In general, MXenes with shorter etching times and less hydrofluoric acid concentrations exhibit higher electronic conductivity and have better lateral sizes [84,85]. Titanium-based MXene plates with a contact angle of 27–41° displayed hydrophilicity [71]. MXenes are suitable for thermal dissipation devices based on electrical and energy sources due to their high thermal expansion coefficients, high thermal conductivity, and constant size efficiency [86]. The outstanding mechanical features of 2D MXenes seem to be one of their distinguishing properties. As a result of their powerful M–C and M–N bonds, MXenes exhibit fascinating mechanical characteristics. In studies, MXenes have been found to have elastic constants (c₁₁) more than two times higher than MAX phases [87] and other two-dimensional samples, such as MoS₂. Transition metal atoms' mass and surface terminal groups influence MXenes' mechanical properties. Magnuson and Halim [88] demonstrated that surface terminal groups reduce the bond of Ti–C strength by omitting its charge. It was discovered that the Ti–C bond lengths in Ti₂C–T_x are longer than those in Ti₃C₂T_x, which can affect the elasticity of the material. It was also suggested that enhancing flexibility could be achieved by altering

the binding strength. According to Zhao et al., supercapacitors, structural materials, and other applications should be considered for these materials due to their high mechanical strength. Asymmetric surface functionalization of MXenes can improve their mechanical stability [89].

MXene-based materials show a high specific surface area of at least 1000 m²/g [90] and outstanding electron conductivity. The effective partitioning of photoinduced charge carriers in two-dimensional MXene materials is a key characteristic of these materials as photocatalysts [91]. As MXene has a strong capability of electron capturing and well-ordered e[−]h⁺ separation, photoinduced electrons can transfer from photoexcited semiconductors to MXene when light is irradiated. The present electrons and holes in MXene, can react with O₂ and H₂O and generate radicals of •O₂ − and •OH, respectively, for organic contaminants oxidation [92]. In MXene, photogenerated e[−] breaks through the Schottky barrier and rapidly moves to the surface, allowing photoinduced charges to be separated. As the Schottky barrier prevented photoexcited e[−] from migrating from MXene to the semiconductor, the estranged e[−] concentrated on the surface of MXene for conducting reduction reactions [93]. A Schottky barrier produced via the electric field in the MXene greatly improved its photocatalytic efficiency.

It has been demonstrated that the thickness of Ti₃C₂T_x films was 5 nm and was able to transmit photons at wavelengths between 300 and 500 nm and had transmittances up to 91.2%. Furthermore, a Ti₃C₂T_x film's absorption peaks can also be strong and broad at 700–800 nm, depending on its thickness. Thickening also gives the material a pale green color, which is beneficial for photothermal usage. Interestingly, optimizing the ion incorporation and thickness of the film leads to higher transmittance amounts [94]. The transmittance of Ti₃C₂T_x films was increased from 74.9 to 92% by tetramethyl ammonium hydroxide, whereas it was reduced by hydrazine, DMSO, and urea. It is necessary to establish different optically linked properties for MXene, such as plasmonic emission color, non-linear optical properties, and luminescence productivity, in order to expand its uses [93,95].

4. Removing Pollutants from Wastewater: Challenges and Opportunities

Aside from natural storm runoff, wastewater is primarily generated by activities of anthropogenic, such as the mismanagement of agriculture and industrial effluent [96–98]. There are many hazardous contaminants present in wastewater, involving organic and inorganic contaminants, heavy metals, poisonous materials, microplastics, and complex poly-structured derivatives, which can be a threat to humans and the environment [4,99–102]. Although heavy metals and complex organic materials are found in low quantities in the effluent, they are the most hazardous to human health [103]. A variety of methods are employed for cleaning wastewater at both the laboratory and industry levels. These involve adsorption [104,105], sand filtration, membrane, advanced oxidation [106], biological treatment, reverse osmosis (RO), ion exchange, photocatalysis, etc. [107–111]. By combining these approaches in wastewater purification, toxic wastes and heavy metals can be degraded more quickly [112,113]. Physicochemical and biological degradation have been used to omit harmful substances from wastewater. The use of chemical methods usually generates a large amount of secondary pollution, which must be removed by a secondary treatment process [114]. Special equipment and high operational costs are required for the filtration process [115]. Solid sludge generated by biological treatment methods requires additional setup for disposal or incineration [116,117]. A nanomaterial has many remarkable features, involving tiny size, high surface area, great movability, flexibility, biocompatibility, and powerful adsorption capabilities. Several nanomaterials, including metal and metal oxide nanoparticles [105,118,119], carbonaceous nanomaterials [120], nanopolymers [121], nanocomposites [122], and nanogels [123], have been employed for pollution remediation.

5. Pollutant Removal with MXenes in Wastewater via Adsorption

Nanomaterials based on MXene have emerged as promising adsorbents for wastewater pollution control [11,124–128]. These adsorbents exhibit interesting physicochemistry, such as high surface areas, hydrophilicity, great adsorption capacities, electron density, available sites for adsorption, effective ion exchange, as well as activated metallic OH sites. MXenes have strong redox reactivity, making them versatile catalysts for electrocatalytic and photocatalytic pollution removal [129,130]. In addition to being inexpensive, safe, and abundant, MBNs can be prepared efficiently, allowing them to be used frequently for environmental remediation [131].

5.1. Adsorption of Inorganic Contaminant

This part discusses the adsorption process of inorganic contaminants such as copper (Cu), mercury (Hg), lead (Pb), and chrome (Cr) from wastewater, and their removal mechanism is demonstrated in Figure 3. In Table 2, different kinds of MXene are illustrated for the removal of the metals.

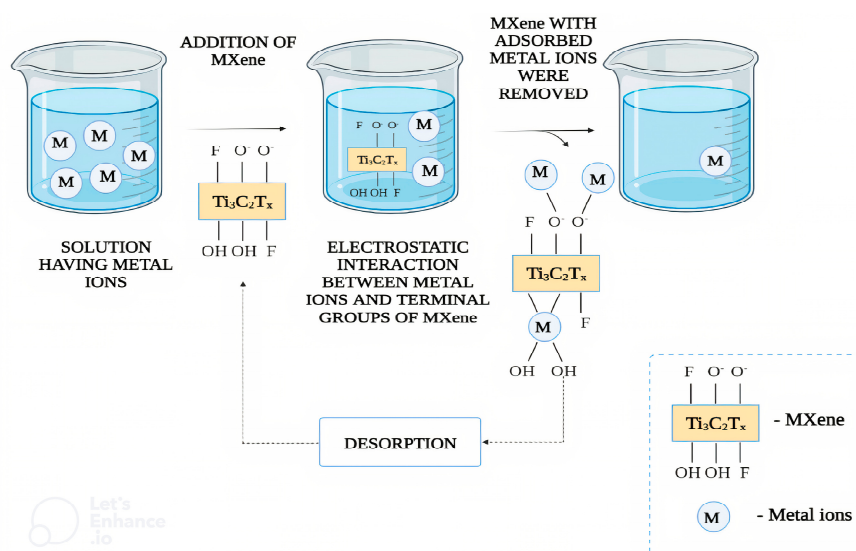


Figure 3. Metal ions adsorption by MXene [132].

Table 2. Application of MXene in heavy metals removal.

2D MXene	Contaminants	Adsorption Duration	Adsorption Capacity	Ref.
Ti ₃ C ₂ T _x -KH570	Pb	2 h	147.290 (mg/g)	[111]
Ti ₃ C ₂	Cr(VI)	14 h	80 (mg/g)	[112]
Ti ₃ C ₂ T _x MXene Nanosheets	Cu	1 min	78.4 (mg/g)	[113]
Magnetic Ti ₃ C ₂ T _x Nanocomposite	Hg	24 h	1128.41 (mg/g)	[114]
Ti ₂ C ₂ T _x	Pb	2 h	36.6 (mg/g)	[115]

5.1.1. Lead Adsorption

The industrial process of mining, color manufacturing, fertilizer production, batteries, and metal plating regularly discharges lead, which is among the most dangerous harmful contaminants. There is a wide variety of applications for MBNs as excellent adsorbents with a high capacity for the adsorption of lead [131]. By chemically exfoliating MXene and intercalating alkali, 2D alk-MXene is produced (Ti₃C₂(OH/ONa)_xF_{2-x}). The two-dimensional alk-MXene adsorbent exhibited promising results in the decomposition of lead, in which the adsorption capacity (AC) reached 140.10 mg/g, achieving adsorption

equilibrium after 2 min. Using hydrofluoric acid, MXene was prepared from Ti_3AlC_2 . A mixture of MXene and alginate powder was prepared, filling the interlayer spaces and enabling lead adsorption. MXene/alginate composite demonstrated an enhanced AC of 382.70 mg/g and reached equilibrium during a quarter-hour [133].

5.1.2. Chromium Adsorption

The second inorganic contaminant is chromium, which is generated by factories such as leather tanning, refractories, electroplating, and metallurgy. There are two natural forms of chromium: trivalent—Cr (III) and hexavalent—Cr (VI). The chromium forms serve as a nutrient for aquatic living beings. However, it is toxic at high concentrations. The hexavalent chromium Cr (VI) is classified as a carcinogenic agent. Therefore, chromium ions must be removed from the environment before they can be discharged [131]. An overview of some results obtained using MBNs as absorbents is presented in this section. To produce two-dimensional $\text{Ti}_3\text{C}_2\text{T}_x$ nanosheets, bulk $\text{Ti}_3\text{C}_2\text{T}_x$ was etched using HF solution and ultrasonically delaminated. Cr (VI) ions adsorption from the effluent was excellent with the obtained $\text{Ti}_3\text{C}_2\text{T}_x$ nanosheets. During the analysis of purified water, it had a concentration of about 5ppb and an AC of 250.0 mg/g. In addition, Cr (III) ions were found to be decreased to a less harmful form [48]. An in situ polymerization and intercalation process was used to functionalize MXenes using poly (m-phenylenediamine) (PmPD). The $\text{Ti}_3\text{C}_2\text{T}_x$ /PmPD nanocomposite exhibits improved hydrophilicity, enhanced spacing between layers, positive surface charge, and more surface area than $\text{Ti}_3\text{C}_2\text{T}_x$ as well as PmPD. A good AC of 540.40 mg/g has been reported for the nanocomposite, almost 4 times as large as that of the non-functionalized MXene $\text{Ti}_3\text{C}_2\text{T}_x$. Using an original concentration of 100 ppm, it was discovered to show pseudo-second-order behavior and to be almost 90% effective after 5 cycles of treatment [134]. A nanocomposite of urchin-like rutile TiO_2 -C was fabricated under FeCl_3 conditions via in situ MXene ($\text{Ti}_3\text{C}_2(\text{OH})_{0.8}\text{F}_{1.2}$) phase transformation. In contrast, the unmodified MXene demonstrated 62 mg/g AC, and the nanocomposite showed 225 mg/g for the chromium ion (Cr (VI)). Within 24 h, adsorption equilibrium was reached ($\text{Ti}_3\text{C}_2(\text{OH})_{0.8}\text{F}_{1.2}$) [135]. A primary rationale for the use of MXene as a novel sorbent to get rid of Cr^{+6} is provided by Ying et al. The representative indicates that Cr^{+6} adsorbs on $\text{Ti}_3\text{C}_2\text{T}_x$ by the natural act of concluded $-\text{OH}$ moieties, followed by a modification of Cr^{+6} sorption to Cr^{+3} , and finally, outer layer co-precipitation of $\text{Cr}(\text{OH})_3$. There was a wide variation in the removal potency between $\text{TiO}_2/\text{Ti}_3\text{C}_2(\text{OH})_{0.8}\text{F}_{1.2}$ (225 mg/g) and $\text{TiO}_2/\text{Ti}_3\text{C}_2(\text{OH})_{0.8}\text{F}_{1.2}$ at a hydrogen ion concentration of 5.0. The synergistic action of nZVI alk- Ti_3C_2 nanosheets is responsible for the high removal potency of MXene/nZVI under acidic circumstances (pH = 2.0) [48].

Moreover, MXenes were utilized as adsorbents to eliminate Cr(VI) and methyl orange (MO) from water. According to the result, the rate of Cr(VI) and MO removing was fast, and the kinetic system followed the pseudo second order; the sorption isotherm was closely aligned with the Langmuir isotherm, and the highest removing efficiency for Cr(VI) and MO achieved 104 and 94.8 mg/g. It was possible to regenerate MXenes using NaOH 0.1 M aqueous solution, and the process was repeated many times. MXenes typically absorb Cr(VI) and MO via chemical adsorption in four different ways (Figure 4) [136].

5.1.3. Copper Adsorption

The production of paper, pharmaceutical products, batteries, mining, and fertilizer have been reported as sources of copper ions. Whenever sewage is discharged from these kinds of industries into the environment, it negatively affects humans and the environment [137]. MXene nanosheets $\text{Ti}_2\text{C}_2\text{T}_x$ that contain oxygenated functional groups were used to effectively remove copper ions. The study by [138] indicated that delaminated MXene showed superior AC than multilayered MXene. It indicated a capacity of 78.450 mg/g for adsorption. More than 79% of the contaminants were adsorbed in 60 s, and the adsorption equilibrium was reached in under 3 min. The efficiency of adsorption, after retaining three cycles, got reduced [139]. MXene $\text{Ti}_3\text{C}_2\text{T}_x$ was delaminated, and the TiO_2 rutile phase

was delaminated by reacting with the amino acids that existed in the solution. The resulting reaction formed a histidine-functionalized rutile TiO_2 DL- $\text{Ti}_3\text{C}_2\text{T}$ hybrid. The produced material could achieve approximately 94.6 mg/g of AC. In 5 minutes, 75% of the Cu ions were omitted. It was also found that MXene functionalized with amino acids enhanced removal efficiency [140]. Using $\text{Ti}_3\text{C}_2\text{T}_x$ powder, ultrasonication was conducted, and DOPA solution was added under magnetic stirring to prepare $\text{Ti}_3\text{C}_2\text{T}_x$ -PDOPA composites. The composite AC obtained 46.60 mg/g, and the maximum adsorption capability was 93.20%. Pseudo-first-order kinetics fit the adsorption data. Due to the functional groups of DOPA, $\text{Ti}_3\text{C}_2\text{T}_x$ was more effective when it was used as an adsorbent [141].

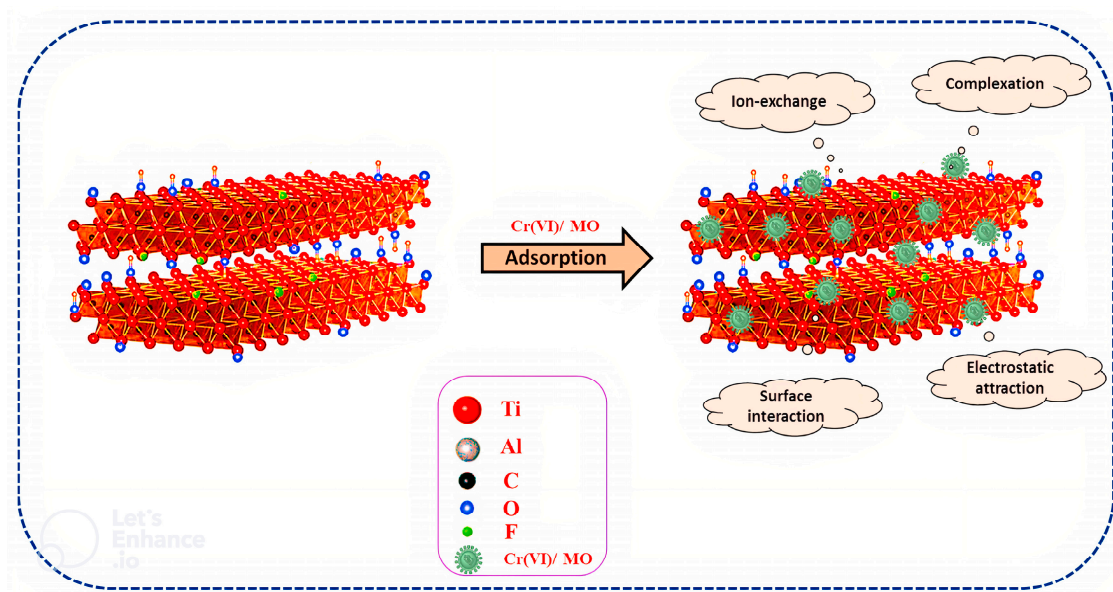


Figure 4. Degradation of Cr(VI) and MO by MXenes [136].

5.1.4. Mercury Adsorption

The toxic metal mercury is included in the top 10 most poisonous materials. Coal and waste burning are the leading causes of mercury pollution. Aside from battery production, mining, cement, and paper production are also industrial sources. The nervous system is susceptible to its effect. Therefore, mercury must be removed, at least to a safety level [131]. MBNs have been used to remove mercury from water in some studies. Hydrothermal treatment and ultrasonication were used to functionalize $\text{Ti}_3\text{C}_2\text{T}_x$ MXene nanosheets with nanolayered molybdenum disulfide. By combining oxygenated terminal groups with disulfide groups, mercury ions were removed through adsorption. Using a novel MoS_2 - $\text{Ti}_3\text{C}_2\text{T}_x$ nanocomposite with increased degradation efficiency, it was possible to reduce the concentration of mercury ions from 50 $\mu\text{mol/L}$ to 0.01 $\mu\text{mol/L}$ within 2 min. Based on Langmuir adsorption isotherm, an AC of 7.160 mmol/g was reached by the composite. Moreover, mercury ions were removed at ppb levels even when metal ions were present [142]. MXene core-shell aerogels (MX-SA) were fabricated using different $\text{Ti}_3\text{C}_2\text{T}_x$ MXene and sodium alginate concentrations. The MX-SA4:20 composition showed excellent mercury ion adsorption among the different compositions. Approximately 932.84 mg/g of Hg ions can be adsorbed by it. For Hg ions, it has an efficiency of 100%, while for other metal ions, it has an efficiency of greater than 90%. Within 15 min, the concentration of Hg reached 1.8 ppb, according to the study. In acidic conditions, it is excellent at removing pollutants [53]. There was a maximum AC of 4806.0 mg/g for multi-layered oxygen-functionalized Ti_3C_2 ($\text{Ti}_3\text{C}_2\text{O}_x$). The degradation efficiency of almost 95.6% was achieved with the oxygen-functionalized multi-layered Ti_3C_2 ($\text{Ti}_3\text{C}_2\text{O}_x$) when the concentration was decreased from 10,400 to 33 g/L [143].

5.1.5. Mechanisms of Heavy Metals Degradation

A variety of mechanisms explains the heavy metals' adsorption on surfaces of MXene. There is a great affinity between titanium and several metal ions. MXenes with large surface areas may trap metal ions in their layered structure. Furthermore, electrostatic interactions occur when metal ions and functional groups on MXene surfaces exchange ions. A Freundlich model signifying multilayer adsorption describes the isotherm data of heavy metal removal from most MXenes.

MXene surface can be charged positively at low pH owing to abundant protonated hydroxyl groups, through which it attracts the negatively charged $\text{Cr}_2\text{O}_7^{2-}$ ions via electrostatic attraction. After the Cr(VI) adsorption of ions onto the surface, the reduction of Cr(VI) to Cr(III) takes place due to the transfer of electrons from $\text{Ti}_3\text{C}_2\text{T}_x$ to Cr(VI). A [Ti–O] bond between $\text{Ti}_3\text{C}_2\text{T}_x$ and Cr(III) ions may cause the ions to be adsorbed to the $\text{Ti}_3\text{C}_2\text{T}_x$ with high affinity. During the formation of covalent bonds (Ti–O–Cr(III)) between Cr(III) ions and MXene, the Cr(III) ions attach to the surface [144]. The adsorption mechanism of Pb(II) ions on Ti_2CT_x -enzymatic hydrolysis lignin (EHL) is illustrated in Figure 5. The Pb ions are mostly adsorbing onto the surface of the MXene nanosheets and EHL because of the exchange of ions and chelation of ions via functional groups and polycyclic structures on the Ti_2CT_x nanosheets surface. Through chemisorption, Pb ions interact by surface groups such as –OH and –COOH to enhance the adsorption [145].

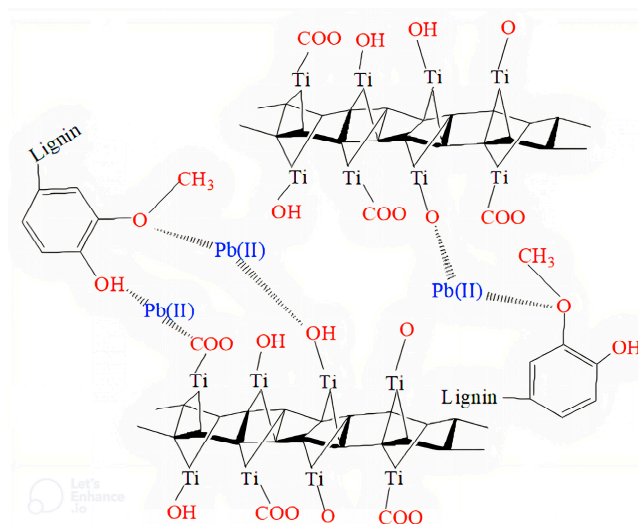


Figure 5. Removal mechanism of Pb(II) ions with Ti_2CT_x -EHL [145].

5.2. Adsorption of Organic Contaminant

MBNs can also remove organic pollutants in addition to inorganic contaminants. The textile industry discharges a significant amount of wastewater containing dyes. In most studies, MXenes and MXene-based materials were reported to be efficient at adsorbing and reducing the cationic dye, MB, but other dyes were also reported to be removed, such as Rhodamine B [146], Safranin T (ST) [147], Acid blue 80 (AB80) [148], MO [149,150], and Neutral red (NR) by MXenes [147].

Many studies have focused on methylene blue so far. Several findings are discussed here. With an easy and scalable approach, Ref. [151] developed porous MXene/single-walled carbon nanotubes. Utilizing the produced material as a dependent electrode, MB was decomposed by AC of 55.80 mg/g; by electro-sorbing, MB was degraded with a great AC of 1068.80 mg/g at 1.2 V applied voltage. The maximum AC was also reported to be 28,403.70 mg/g. Additionally; selective adsorption can remove MO by optimizing the pH. A composite made of PA and MXene was prepared through the hydrothermal preparation of mixing MXene and PA at different concentrations. Adsorption capacities of 42 mg/g for MB and 22 mg/g for rhodamine B were observed for PA-MXene-12 composites. Because of

its larger surface area and O₂-containing functional groups, the composite showed a higher level of adsorption. An increase in pH from 3 to 11 increased the capacity of adsorption and reached 106.70 mg/g. Even after 12 continuous cycles, it retained nearly 85% of the removal efficiency [152]. During the synthesis of MXene, the etching technique also affects dye adsorption. A comparison between Ti₃C₂ prepared by HF etching and Ti₃C₂ synthesized via hydrothermal route was conducted by Peng et al. [150] for MB and MO dye adsorption. Although, both MXene preparations could not adsorb MO on a practical level. MXene prepared by the hydrothermal method exhibited considerably higher MB adsorption than MXene prepared by HF etching. This is likely because of their large specific surface area as a result of efficient etching and exfoliation.

Table 3 shows the different surface-modified MXene-based nanomaterials utilized to remove dyes. It is also possible to remove pharmaceutical compounds using nanomaterials based on MXene. MXene was used to remove the drug amitriptyline (AMT) with a superior AC of 58.70 mg/g. Although sonication increases the efficiency of adsorption [153].

Table 3. Utilizing of MXenes for dye removal.

2D MXene	Contaminants	Adsorption Duration	Adsorption Capacity	Ref.
KOH-Ti ₃ C ₂ T _x	MB	-h	77 (mg/g)	[136]
Ti ₃ C ₂ T _x	AB80	20 h	-	[130]
Self-assembled MXene (Ti ₃ C ₂)-Co ₃ O ₄ nanocomposite	Rhodamine B	700 min	47.68 (mg/g)	[128]
Ti ₂ C ₂ T _x	MB	0–24 h	140 (mg/g)	[115]
Sulfonic groups functionalized MXenes (Ti ₃ C ₂ -SO ₃ H)	MB	70 min	111.1 (mg/g)	[137]
MXene (Ti ₃ C ₂ (OH _x F _{1-x}) ₂)	ST	180 min	2.861	[129]

Mechanisms of Heavy Metals Degradation

MXenes adsorb dye molecules primarily through interactions with molecules of dye and the functional groups on their surface. An illustration of the proposed mechanism for MB adsorption on MXene@Fe₃O₄ can be seen in Figure 6 [47]. The molecules of MB⁺ bind to hydroxyl groups on Ti surfaces for ionizing H⁺ and generate a monodentate complex via the M–O–H...N bond, as shown in Equations (1) and (2).

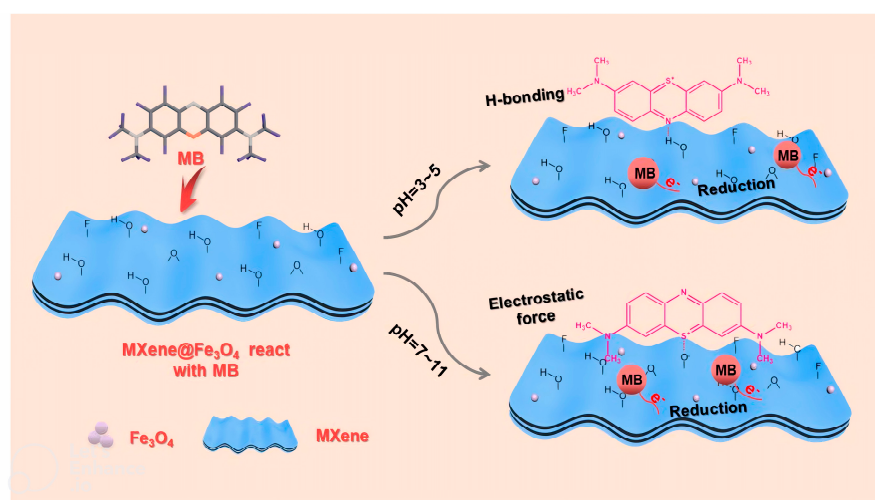


Figure 6. Suggested mechanism for MB adsorption by MXene@Fe₃O₄ [154].

Electrostatic adsorption of MB promotes complex formation, whereas electrostatic adsorption of MB^+ and positive charges on the surface of $\text{MXene@Fe}_3\text{O}_4$ impedes it. Because of interactions among the OH group and the Ti site, MB is possibly reduced by $\text{Ti}_3\text{C}_2\text{T}_x$ nanosheets and adsorbed onto the $\text{MXene@Fe}_3\text{O}_4$ surface. A dipole–dipole H-bonding interaction also exists among the N of the MB and the Ti–OH group, which forms an $\text{OH}\cdots\text{N}$ bond. Based on the investigation of Li et al. [147], MB adsorption on $\text{MXene-COOH@PEI/PAA}_n$ core–shell nanocomposites occurs in three stages: surface adsorption, internal diffusion of particles, and equilibrium adsorption. Adsorption and subsequent photocatalytic decomposition remove cationic dye MB by $\text{MXene} (\text{Ti}_3\text{C}_2\text{T}_x)$ [148]. $\text{Ti}_3\text{C}_2\text{T}_x$ can remove MB in several steps. The first stage involves the MB adsorption on $\text{Ti}_3\text{C}_2\text{T}_x$ surfaces, increasing stacking disorder, possibly because of the wedged layer structure or chemical MXene transformations. The final step results in the formation of titania when $\text{MXene} (\text{Ti}_3\text{C}_2\text{T}_x)$ is oxidized. Alternatively, the dye may be degraded via photocatalysis under UV illumination, possibly because of the $\text{Ti}(\text{OH})_4$ and/or TiO_2 formation on surfaces of MXene .

6. Combining Fenton Method with MXene-Based Materials for Organic Pollutants Degradation

In recent years, oxidation with the Fenton approach has been broadly investigated because of its high productivity, operation simplicity, and lack of subordinate pollutants [155–158]. There are two common oxidants used in Fenton-like systems: H_2O_2 and PS. In particular, MXene -based catalysts are usually conductive and possess abundant active sites, making them effective catalysts for degrading organic pollutants with $\text{H}_2\text{O}_2/\text{PS}$ [159].

6.1. Oxidation of H_2O_2 Activated by MXene

The oxidation of H_2O_2 has attracted broad interest in removing organic contaminants. [160], where the Fe^{2+} ions produce free radicals as a catalyst [161]. In addition to having a lamellar structure, the 2D MXene also has surface electronegativity. Two-dimensional MXene could be loaded with particles of iron both on the surface and within lamellar spaces [162]. Furthermore, MXene can disperse iron nanoparticles constantly, effectively inhibiting the accumulation of iron nanoparticles [163]. Iron particles loaded into 2D MXene possess a larger specific surface area and a good porous construction rather than sheer 2D MXene .

For the H_2O_2 activating, the pores in the complex might act like microreactors. Ranitidine was removed by H_2O_2 activated by magnetic $(\text{nZVI})@\text{Ti}_3\text{C}_2$ nanosheets in 30 min with 91.1% removal efficiency [164]. Thus, MXene -loaded iron species are an effective catalyst for degrading organic pollutants.

Presently, Fe_3O_4 , MnFe_2O_4 , and nZVI are mainly used as iron-based particles. A significant factor that affects the activity of 2D MXene is the mass ratio of iron species to MXene . For example, ferric acetylacetonate was used to modify 2D MXene in different ratios. With increasing mass ratio, methylene blue's degradation efficiency increased first, then decreased. By increasing the mass ratio from 2:1 to 1:1, the catalyst's pore structure and specific surface area were improved. Additionally, the accumulation of excessive Fe_3O_4 reduced specific surface area and active site content as the mass ratio increased [161].

Mechanisms of H_2O_2 Activation with MXene-Based Materials

A 2D MXene surface coated with iron particles could provide more reaction sites. MXene can facilitate the transfer of electrons among magnetic particles. Additionally, MXene/nZVI nanosheets contain many hydrophilic functional groups, such as OH, $-\text{COOH}$, and $-\text{CHO}$, which promote the activation of H_2O_2 [164]. An illustration of the possible mechanisms by which organic pollutants can be degraded in iron-based $\text{MXene}/\text{H}_2\text{O}_2$ systems is given in Figure 7. These four kinds of reactions are explained below. (1) Oxidation of H_2O_2 on the surface of iron-based MXene : $=\text{Fe}^{2+}$ possesses excellent reduction potential, increasing the rate of H_2O_2 reduction and promoting the degradation of organic molecules.

("=" indicates the element connected to the surface of MXene). (2) Oxidation of H_2O_2 in solution: iron particles precipitate into the solution from the surface of Fe-based MXene, becoming free Fe^{2+} needed for H_2O_2 activation. (3) Straight reduction: $=\text{Fe}^{3+}/\text{Fe}^{3+}$ is reduced into $=\text{Fe}^{2+}/\text{Fe}^{2+}$. In addition, $=\text{Fe}^{3+}/\text{Fe}^{3+}$ can have a reaction by H_2O to produce $\text{O}_2\cdot^-$ and enhance the decomposition of organic compounds. (4) Indirect reduction: hydrogen atoms are formed in the environment by a reduction reaction of free hydrogen ions. The hydrogen ions could mix with $=\text{Fe}^0$ to produce active particles such as $=\text{Fe}^0\cdot[\text{H}]$. Moreover, $=\text{Fe}^{2+}$ can be produced by reacting active particles by $=\text{Fe}^{3+}$. Lastly, organic matter reacts with $\cdot\text{OH}/\text{O}_2\cdot^-$ and $=\text{Fe}^0\cdot[\text{H}]$.

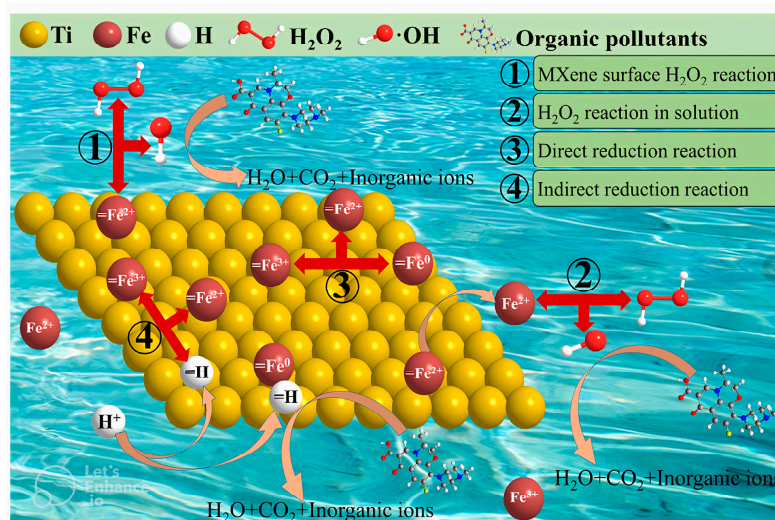


Figure 7. An investigation of the possible mechanism by which 2D MXene/ H_2O_2 can degrade organic pollutants [165].

6.2. Utilizing MXene-Based Materials to Activate PS

A great deal of interest has been expressed in the field of organic pollutants degradation based on persulfates (PS) [166]. Generally, PS can be classified into two groups: peroxymonosulfate (PMS, HSO_5^-) and peroxodisulfate (PDS, $\text{S}_2\text{O}_8^{2-}$) [167]. Additionally, PMS and PDS have oxidation potentials of 1.82 and 2.01, respectively [168]. By activating PMS and PDS, pollutants could be degraded via free radicals and non-radical routes such as the transfer of electrons [169].

Mechanisms of Activating PMS

The use of MXene-based materials for activating peroxymonosulfate has multiple advantages [170]. MXene's multilayer structure and high surface area can enable active sites to be fixed [171]. Secondly, MXene's high reducibility prevents the active sites aggregation within catalysis, resulting in increased efficiency [172]. Further, MXene has an excellent specific capacity [173], which promotes the movement of electrons between the interface and the PMS.

There are many reductive active sites in the 2D MXene/metal complex and good PS activity (Figure 8). Combining PMS with metal atoms makes electrons move faster from peroxymonosulfate to the MXene surface, activating peroxymonosulfate [174]. For PMS activation, zero-valent iron nanoparticles (nZVPIs)/MXene were fabricated. PMS connected to Fe particle and 2D MXene resulted in the elongation of the $\text{I}_{\text{O-O}}$ bond. This demonstrated that there are two active centers in the catalyst. Furthermore, two-dimensional MXene or Fe particles react easily with PMS with a low energy barrier [175]. Additionally, secondary pollution was reduced because metal ions were less likely to leach into the solution.

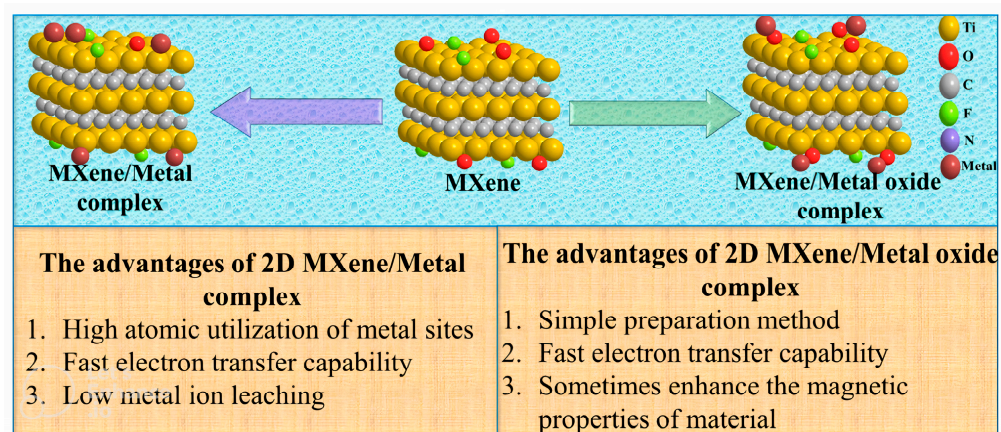


Figure 8. The benefits of MXene/Metal and MXene/Metal oxide complex in the system of PS [165].

Two-dimensional MXene might serve as a connection platform for metal oxides. It is simple to fabricate MXene/metal oxide complexes. In some cases, metal oxides increase the magnetism of complexes for ease of reclaiming (Figure 8). Furthermore, single MXene or metal oxides have lower PS catalytic abilities than MXene/metal oxides. For instance, $\text{CoFe}_2\text{O}_4/\text{MXene}$ improved PS activating than CoFe_2O_4 , causing the Co/Fe/Ti complex formation to enhance the reactions of the valence cycle of Co(II)/Co(III), Fe(II)/Fe(III), and Ti(II)/Ti(IV). Therefore, the electron movement was enhanced, and the pollutant decomposition rate was improved [176]. There is a significant increase in PS activation following the MXene complexation with metal oxides (Figure 8). Furthermore, metal ions react via functional groups of surface such as -O, -OH, and -F to make durable complexes of metal/Ti, accelerating redox reactions [177].

MXene's dimension is associated with its capability of activation. Because monolayer MXene contains more exposed active sites, it has a superior PS activation capability than bulk MXene. Unlike multilayer 2D MXene bulk, monolayer 2D MXene also possesses a minor HOMO-LUMO gap, facilitating electron transfer and generating free radicals. Single-layer MXene, for example, degrades aqueous 2,4-dichloro phenoxy acetic acid at an exponential rate 376 times faster than bulk MXene ($7.8 \times 10^{-4} \text{ min}^{-1}$) [178]. To improve PMS activity, monolayer 2D MXene must be prepared and optimized. As shown in Figure 9, MXene-based catalysts can activate PMS, and organic compounds can be degraded by different mechanisms. (1) Activating PMS by =Ti relative active sites can degrade different mechanisms. Firstly, =Ti^{2+} and =Ti^{3+} lose e^- to produce =Ti^{4+} , forming particles for oxidizing [179]. In the second step, the =Ti^{3+} on the surface of MXene can react via PMS to generate $\text{SO}_4^{\cdot-}$. Furthermore, =Ti and transition metals on the MXene surface sustain redox reactions to promote electron movement. MXene could facilitate the Cu(II)/Cu(I) cycle, which makes PMS to be active in generating many oxidative particles, such as $\text{SO}_4^{\cdot-}$, and HO^{\cdot} , $^1\text{O}_2$ [180]. Moreover, terminal =Ti-F and the unsaturated =Ti-C-O are significant active sites for activating PMS [181]. Thus, =Ti is a significant active site for PMS activation [175]. (2) Two-dimensional MXene surface terminals (-O, -OH) could make active sites, thereby activating PMS to produce radicals, including $\text{O}_2^{\cdot-}$, $\text{SO}_4^{\cdot-}$, and $^1\text{O}_2$. Additionally, metal sites on the surface of MXene are capable of adsorbing PMS and activating it to produce $\text{O}_2^{\cdot-}$. (3) There are also several dissolved metal ions in H_2O that can activate peroxymonosulfate, and the most predominant oxidizing particles can be $\text{SO}_4^{\cdot-}$ and OH^{\cdot} [182]. The major active particles are $\text{SO}_4^{\cdot-}$, OH^{\cdot} , and $^1\text{O}_2$ with activating peroxymonosulfate [183].

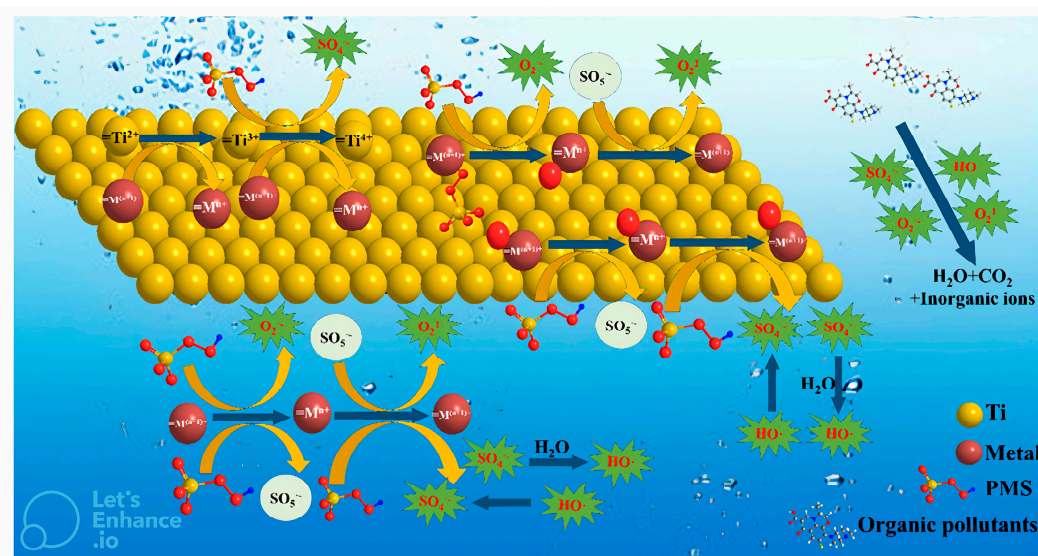


Figure 9. Using MXene-based catalyst and PMS for the decomposing of organic contaminants [165].

The activation of PDS can result in free radical generation as well as non-radical oxidation [184]. MXene-based materials show excellent electrical conductivity, meaning they could be used to activate PDS by transferring electrons. Furthermore, it has been demonstrated that the metal sites on the surface of MXene can activate PDS to generate $\text{SO}_4^{\bullet-}$, $\cdot\text{OH}$, $\text{O}_2^{\bullet-}$, and $\text{S}_2\text{O}_8^{\bullet-}$, which can be used to purify water by combining with organic pollutants.

7. An MXene-Based Photocatalysis System for Pollutants Removal in Wastewater

MXene materials possess an excellent application outlook in photocatalysis due to their surfactants, electron movement features, and in situ oxidation properties. In research on the conversion of CO_2 , water purification, contaminants decomposition, etc., MXene materials have been broadly utilized for their photocatalytic properties. Currently, photocatalytic water purification materials are not practical because of the catalyst's high price, weak reusing of materials, less usage and sunlight conversion, trouble transferring small-scale decomposition to large-scale applications, and unclear catalytic mechanisms. The countries have consistently emphasized water resources recently, which calls for developing new water treatment technologies. Many research projects have also been started using MXene materials for photocatalytic water treatment [185–190].

7.1. Composite Based on MXene/ TiO_2

An N-doped porous two-dimensional layered $\text{TiO}_2/\text{Ti}_3\text{C}_2$ MXene photocatalyst with exceptional stability, excellent electron movement, and superior visible-light photocatalytic performance was tested for phenol decomposition [191]. For three hours, phenol degradation was detected at 10%, 38.70%, and 96% in different samples containing TiO_2 , $\text{TiO}_2/\text{Ti}_3\text{C}_2$ MXene, and N-doped $\text{TiO}_2/\text{Ti}_3\text{C}_2$ MXene. N-doped $\text{TiO}_2/\text{Ti}_3\text{C}_2$ MXene removed phenol by trapping free radicals using $\text{C}_6\text{H}_4\text{O}_2$, $\text{C}_4\text{H}_{10}\text{O}$, and $\text{C}_{10}\text{H}_{16}\text{N}_2\text{O}_8$, which acts as $\cdot\text{O}_2^-$, $\cdot\text{OH}$, and h^+ scavengers, $\text{C}_4\text{H}_{10}\text{O}$ and $\text{C}_{10}\text{H}_{16}\text{N}_2\text{O}_8$ moderately reduced the amount of phenol removal, while p-benzoquinone significantly reduced phenol degradation. The findings show that the degradation process is influenced by $\cdot\text{O}_2^-$, $\cdot\text{OH}$, and h^+ . N-doped TiO_2 creates photogenerated electrons (e^-) and holes (h^+), which rapidly moved to the N-doped C matrix under visible-light irradiation. Compared to C (-0.08 eV), TiO_2 has a relatively larger conduction band (CB) (-0.3 eV) [192], which enhances C conductivity to take on photoinduced e^- , increasing separation ability [193]. By reacting photoinduced electrons with O_2 , $\cdot\text{O}_2^-$ can be generated, and reacting photo-induced holes with OH^- in

H₂O causes the production of $\cdot\text{OH}$ [194]. Figure 10 illustrates the photocatalytic phenol removal utilizing N-doped TiO₂/Ti₃C₂ MXene under visible light illumination.

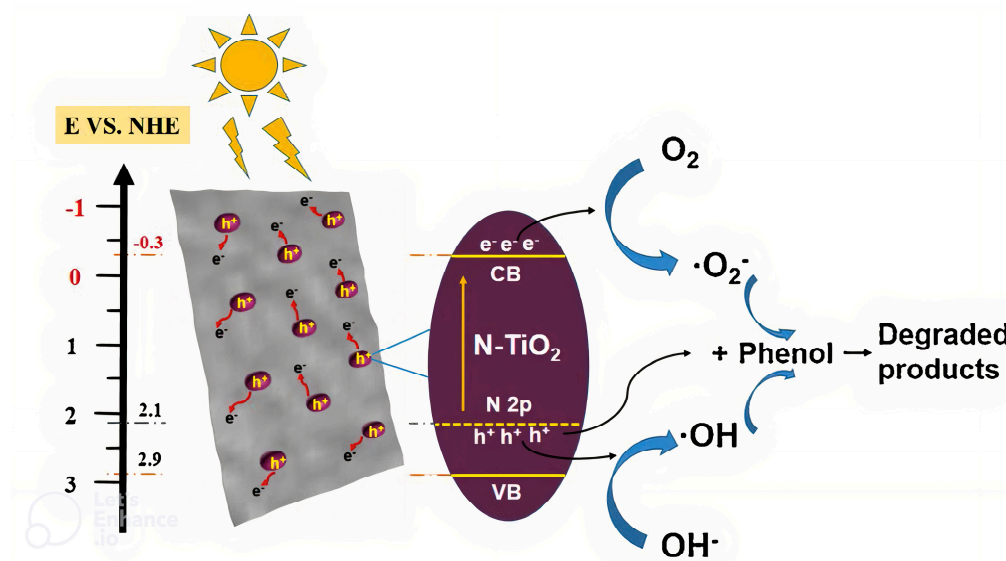


Figure 10. Photocatalytic phenol decomposition via N-TiO₂@C [191].

Titanium-carbon nanosheets were assessed for photocatalytic decomposition of MB under ultraviolet light irradiation [195]. Compared with perfect TiO₂ nanoparticles, titanium-carbon nanosheets have more outstanding adsorption capabilities. Within 6 h of ultraviolet irradiation, titanium-carbon nanosheets and pristine TiO₂ degraded methylene blue at 86% and 69%, respectively. In high-energy ball milling, titanium-carbon nanosheets exhibit enhanced photocatalytic activity for the following reasons: (1) titanium-carbon nanosheets exhibit exceptional structural properties that promote photocatalysis; (2) a uniform immobilization structure of TiO₂ nanoparticles is evident in titanium-carbon nanosheets, demonstrating high electrical conductivity; (3) titanium-carbon nanosheets developed by oxygen–titanium–carbon chemical bonding could reduce the e^- - h^+ recombination in TiO₂ nanoparticles that are exposed to the light; (4) the Ti³⁺ ions present in TiO₂ could serve as both electron traps and donor sites [196]; (5) thus, e^- activated by photoexcitation at these sites can enhance charge carrier density in photocatalysts [197]; (6) moreover, the unutilized activated Ti³⁺ states trap e^- and, therefore, prevent photogenerated e^- - h^+ pairs from recombining [198]; and (7) the presence of some surface imperfection indicating vacancies of TiO₂ with O₂ reduce the TiO₂ band gap, which may reduce the chance of recombination of e^- - h^+ [195].

Based on the decomposition of MO, the photocatalytic activity of In₂S₃/TiO₂@Ti₃C₂T_x nanohybrids was assessed and compared with other In₂S₃-based catalysts, including In₂S₃/carbon nanotube, In₂S₃/reduced GO, In₂S₃/MoS₂, and In₂S₃/TiO₂ [194]. By modifying In₂S₃/TiO₂ nanohybrids with Ti₃C₂T_x, MO was degraded almost 1.5, 1.5, 2, and 7 times faster than by In₂S₃/TiO₂, In₂S₃/MoS₂, In₂S₃/carbon nanotube, and In₂S₃/GO, respectively. The following reasons could explain the various photocatalytic performances. The work function of Ti₃C₂T_x MXene is very low (1.6–2.8 eV), significantly lower than the work function of In₂S₃/reduced graphene oxide (4.9–5.20 eV), CNT (5.10 eV), MoS₂ (4.0 eV), and TiO₂ (4.90 eV) [199]. The improved synergetic double heterostructure and Ti₃C₂T_x with considerable electrons/holes movability, as well as superior electrical conductivity, facilitate the severance of photogenerated electrons and holes pairs, even though Ti₃C₂T_x contains a considerable volume of functional groups such as O₂, OH, and COOH [200]. After group decoration, CNT and reduced GO generally lose considerable conductivity [201]. The In₂S₃-based catalyst's photocatalytic activity might also be influenced by other param-

eters, such as the amount of precursor, the mass of the particle, the wide surface area, the structure, and the dispersibility of the catalyst catalysts [194].

7.2. MXene and Other Material-Based Composite

Photocatalytic reactions of Ag_3PO_4 result in Ag^+ decomposition; therefore, $\text{Ag}_3\text{PO}_4/\text{Ti}_3\text{C}_2$ nanocomposite has been used to enhance the photocatalytic elimination of a variety of organic pollutants (MO, $\text{C}_6\text{H}_4\text{N}_2\text{O}_5$, tetracycline hydrochloride, $\text{C}_{12}\text{H}_{15}\text{Cl}_2\text{NO}_5\text{S}$, and $\text{C}_{11}\text{H}_{12}\text{Cl}_2\text{N}_2\text{O}_5$) when illuminated by visible light [176]. According to their rate constants (min^{-1}), these compounds degrade in the following order: tetracycline hydrochloride (0.32), MO (0.94), $\text{C}_{11}\text{H}_{12}\text{Cl}_2\text{N}_2\text{O}_5$ (0.25), $\text{C}_6\text{H}_4\text{N}_2\text{O}_5$ (0.005), and $\text{C}_{12}\text{H}_{15}\text{Cl}_2\text{NO}_5\text{S}$ (0.04). The kinds of materials existing in the wastewater, in terms of being organic or inorganic, can have a significant impact on their photodegradation of them. Neither humic acid nor fulvic acid had a significant impact on removing, which is likely because of completion among natural organic materials and tetracycline hydrochloride since humic acid and fulvic acid scavenge $\cdot\text{OH}$ and photo-generated h^+ [202].

On the basis of the decomposition of Congo Red, $\text{BiFeO}_3/\text{Ti}_3\text{C}_2$ was evaluated as a photocatalyst [203]. The photocatalytic degradation of Congo Red in 42 min was approximately 35% in the presence of pure BiFeO_3 . However, when $\text{BiFeO}_3/\text{Ti}_3\text{C}_2$ is present, high levels of Congo Red removal can be achieved (>99%). A dark experiment revealed approximately 20% Congo Red degradation, indicating that a $\text{BiFeO}_3/\text{Ti}_3\text{C}_2$ nanohybrid photocatalyst is superior under dark conditions. As a result of the very stable structure of $\text{BiFeO}_3/\text{Ti}_3\text{C}_2$, the removing performance of the photocatalyst is identical within four-cycle photocatalytic degradation activities. When $\text{BiFeO}_3/\text{Ti}_3\text{C}_2$ is photoexcited, e^- and h^+ are produced. Because $\text{BiFeO}_3/\text{Ti}_3\text{C}_2$ previously described had a relatively low photoluminescence intensity, the Ti_3C_2 nanosheets trap e^- rapidly, reducing the possibility of recombination. Within photocatalytic degradation, e^- reacts with O_2 to generate $\cdot\text{O}_2^-$, and h^+ reacts via H_2O to generate $\cdot\text{OH}$. $\cdot\text{O}_2^-$ and $\cdot\text{OH}$ exhibit high reactivity to the organic pollutants removal, which results in Congo Red being mineralized into CO_2 and H_2O . The increased photocatalytic functioning of $\text{BiFeO}_3/\text{Ti}_3\text{C}_2$ was related to e^- and h^+ great separation times, small crystallite size reductions, and large surface areas of $\text{BiFeO}_3/\text{Ti}_3\text{C}_2$ [203].

Based on the irradiation of visible light, $\text{Ag}_2\text{WO}_4/\text{Ti}_3\text{C}_2$ nanocomposites were evaluated for their photocatalytic properties in removing tetracycline hydrochloride and sulfadimidine [204]. Tetracycline hydrochloride and sulfadimidine degraded 25% and 80% more quickly with $\text{Ag}_2\text{WO}_4/\text{Ti}_3\text{C}_2$ nanocomposites within 40 min than with Ag_2WO_4 particles. The $\text{Ag}_2\text{WO}_4/\text{Ti}_3\text{C}_2$ nanocomposites produce an electrical field that promotes e^- transfer from Ag_2WO_4 to Ti_3C_2 , enhancing photocatalysis [205]. As a result of Ti_3C_2 MXene's metallic conductivity, $\text{Ag}_2\text{WO}_4/\text{Ti}_3\text{C}_2$ nanocomposites exhibit efficient photogenerated charge transfer and have a longer charge-carrier lifespan. To confirm the photocatalytic mechanism, an ammonium oxalate, an isopropanol, and a benzoquinone molecule were utilized to scavenge the photogenerated h^+ , $\cdot\text{OH}$, and $\cdot\text{O}_2^-$, respectively [206]. Researchers found that degrading systems mainly involve holes and $\cdot\text{OH}$, via $\cdot\text{OH}$ having an unimportant role. Previous research has shown that Ti_3C_2 significantly enhances Ag_3PO_4 stability and catalytic performance [176].

$\text{Ti}_3\text{C}_2\text{-OH}/\text{In}_2\text{S}_3/\text{CdS}$ nanocomposites were tested for their photocatalytic properties with decomposing Rhodamine B and MO in visible light [204]. With regard to photodegradation activity, $\text{Ti}_3\text{C}_2\text{-OH}/\text{In}_2\text{S}_3/\text{CdS}$ nanocomposites (approximately 95%) degraded faster than pristine CdS and In_2S_3 catalysts (48% and 54%, respectively) during 8 min. In order to determine the catalytic properties of $\text{Ti}_3\text{C}_2\text{-OH}/\text{In}_2\text{S}_3/\text{CdS}$ nanocomposites, the valence and CB energies of photocatalysts are important factors. CdS and In_2S_3 valence/CB energies were $-0.39/1.70$ eV and $-0.89/1.30$ eV, respectively. When visible light is irradiated on $\text{Ti}_3\text{C}_2\text{-OH}/\text{In}_2\text{S}_3/\text{CdS}$ photocatalyst, the e^- ions are excited to the CB of CdS and In_2S_3 . A $\text{Ti}_3\text{C}_2\text{-OH}$ component in the CdS and In_2S_3 photocatalysts could improve the proper separation of photoinduced e^- – h^+ pairs by transferring photoinduced e^- to $\text{Ti}_3\text{C}_2\text{-OH}$ from the photocatalyst's CB [207]. The generated holes on the valence band (VB)

of the $\text{Ti}_3\text{C}_2\text{-OH}/\text{In}_2\text{S}_3/\text{CdS}$ nanocomposites are powerful in the degradation of organic molecules under the irradiation of visible light [208].

Bismuth oxyhalide photocatalysts are effective in promoting their photocatalytic property through the development of $\text{BiOBr}_x\text{I}_{1-x}$ photocatalysts [209]. An enhanced photocatalytic decomposition rate for Rhodamine B and phenol was obtained by heterostructure $\text{BiOBr}_{0.5}\text{I}_{0.5}/\text{Ti}_3\text{C}_2\text{T}_x$ nanocomposites fabricated using a simple method in comparison to pristine $\text{BiOBr}_{0.5}\text{I}_{0.5}$ and $\text{Ti}_3\text{C}_2\text{T}_x$, and they also showed exceptional chemical stability [210]. The nanocomposites $\text{BiOBr}_{0.5}\text{I}_{0.5}/\text{Ti}_3\text{C}_2\text{T}_x$ degrade almost 100% of Rhodamine B during 40 min and about 50% of phenol during 5 hours under the irradiation of visible light. The same circumstances were applied to $\text{BiOBr}_{0.5}\text{I}_{0.5}$ alone, which omitted just 32% of Rhodamine B and 23% of phenol, respectively, while $\text{Ti}_3\text{C}_2\text{T}_x$ alone did not remove any of the compounds.

Depending on the condition of the solution, $\text{Bi}_{0.90}\text{Gd}_{0.10}\text{Fe}_{0.80}\text{Sn}_{0.20}\text{O}_3/\text{Ti}_3\text{C}_2$ MXene hybrids were appraised like photocatalysts Congo Red removing [211]. In low pH, because of a high concentration of H^+ , hybrid photocatalysts are getting positively charged, while Congo Red with functional groups is charged negatively. A high electrostatic attraction among the molecules and photocatalysts of dye is able to improve dye molecule degradation along with photocatalytic oxidation [212]. However, $\text{Bi}_{0.90}\text{Gd}_{0.10}\text{Fe}_{0.80}\text{Sn}_{0.20}\text{O}_3/\text{Ti}_3\text{C}_2$ MXene hybrids and dye molecules exhibit relatively low electrostatic interaction at $\text{pH} > 3$ as a result of the H^+ concentration in the solution becoming smaller [213].

8. Treatment of Wastewater with MXene-Based Membranes

Water desalination using MXene membranes is a recently developed field of study [110,214,215]. The physicochemical features of MXenes, including their high volumes, hydrophilicity, electrical conductivity, and mechanical strength, set them apart from other 2D materials [216]. In order to implement a membrane for water purification that is highly attractive, MXenes are investigated as they can be used to exploit the distances among layers to enhance ion movement. Around 70 different MXene substances have been utilized to increase the efficiency of supercapacitors and non-aqueous electrolytes for sodium-ion batteries.

8.1. Membrane Made from Pristine MXene

According to Ren et al., a 2D $\text{Ti}_3\text{C}_2\text{T}_x$ membrane was tested in a forward osmosis (FO) system for size-selective rejection and charge of molecules and ions [199]. A membrane that is 1.50 μm thick showed a less permeation rate (10^{-4} mol/h·m²) for several organic dyes and cations, which possessed hydration radii over 6.4 Å. Nanofiltration with dead-end $\text{Ti}_3\text{C}_2\text{T}_x$ membranes was reported by Han et al. [200]. The membrane indicated 115 LMH/bar water flux and a rejection rate of more than 91% for Congo Red, although inorganic salts were rejected by the membrane below 23%. Similar to the 2D material-based membranes that were previously reported, the new 2D membrane neat $\text{Ti}_3\text{C}_2\text{T}_x$ also exhibits a great rejection of subnanometer-scale molecules, permitting the salt ion's permeation.

8.2. Hybrid Membranes Based on MXene

Several studies have been performed on heterostructured MXene membranes, including nanomaterials, to improve performance. A 90-nm-thick $\text{Ti}_3\text{C}_2\text{T}_x$ -GO composite membrane was investigated by Kang et al. (Figure 11) [217]. Adding 30 wt.% GO to thin MXene membranes prevented the non-selective channel formation but did not impact the spacing of the interlayer. The membrane rejected almost 90% of dyes, which were organic with hydration radii over 5 Å, identical to the interlayer space of $\text{Ti}_3\text{C}_2\text{T}_x$ via OH end groups. Using $\text{Fe}(\text{OH})_3$ intercalation, Ding et al. studied the preparation of 400.0 nm thick loosely stacked $\text{Ti}_3\text{C}_2\text{T}_x$ membranes. In order to achieve broader interlayer spaces, the laminated layers were washed in hydrochloric acid to omit the particles of OH [218]. Having a freely stacked construction and large nanochannels, the membrane investigated in this paper exhibited 1084.0 LMH/bar water permeance, which was 5 times more than the water permeance of pristine $\text{Ti}_3\text{C}_2\text{T}_x$ membranes. Despite the broadened nanochannels,

the membrane demonstrated high rejection rates of certain dye molecules, for instance, almost 90% for Evans Blue.

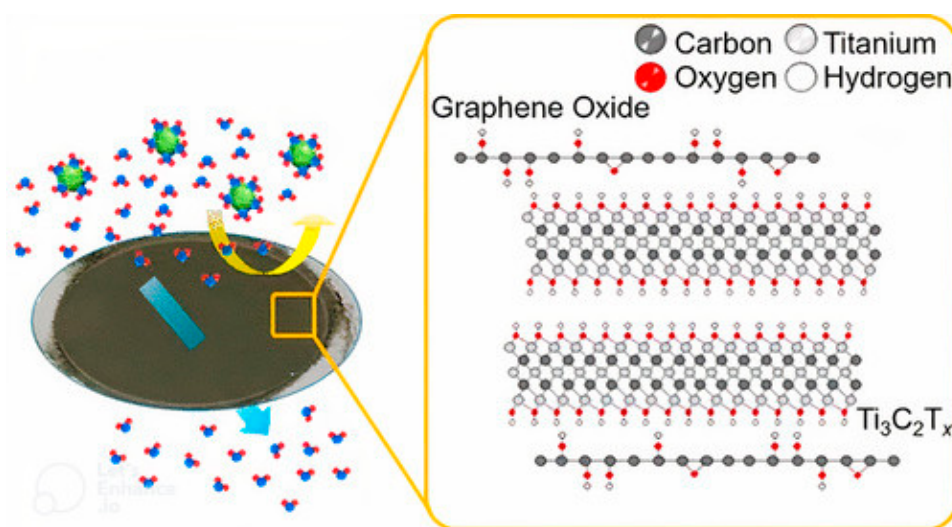


Figure 11. Structure of modified $\text{Ti}_3\text{C}_2\text{T}_x$ -based nanofiltration membranes [217].

A nanofiltration membrane based on Ag nanoparticles and $\text{Ti}_3\text{C}_2\text{T}_x$ was reported by Pandey et al. [219]. Due to the role of $\text{Ti}_3\text{C}_2\text{T}_x$ as a reducing agent, Ag^+ ions are self-reduced, and Ag nanoparticles and nanopores form on the MXene surface, enhancing water movement. The membrane of Ag@MXene indicated increased permeances of 387.0, 354.0, and 345.0 LMH/bar for Rhodamine B, methyl green, and bovine serum albumin, respectively. There were rejection rates of approximately 93% for Rhodamine B, 92.32% for methyl green, and approximately 100% for BSA, which are similar to those of the $\text{Ti}_3\text{C}_2\text{T}_x$ neat membrane. Heterostructured $\text{Ti}_3\text{C}_2\text{T}_x$ MXene membranes with channels incorporating amalgamated CNTs studied by Dine et al. [202]. Due to the presence of CNTs, the fabricated membrane indicated 1270.0 LMH/bar water permeance, whereas a dead-end setup resulted in 97.3% and 100% rejection rates for rose bengal and crystal violet, respectively. Additionally, research has been conducted to improve the sub-nanometer dyes rejection rate and inorganic salts in aqueous environments by prohibiting MXene interlayer spacing from widening. A $\text{Ti}_3\text{C}_2\text{T}_x$ membrane with an Al^{3+} -cation intercalation, for example, was reported by Ding et al. to have great durability in the aqueous solutions [220]. The cation-intercalated $\text{Ti}_3\text{C}_2\text{T}_x$ membranes exhibited restrained swelling in the same condition with great sodium chloride rejection and water flux (1.10–8.50 LMH) in FO procedures more than 400.0 h operation. In a recent study, Lu et al. prepared a self-crosslinked $\text{Ti}_3\text{C}_2\text{T}_x$ membrane through the dehydroxylation of OH groups through thermal treatments (Figure 12) [221]. As a result of its anti-inflammatory capability, the membrane was 20–30 times more effective at excluding monovalent ions than the pristine membranes while used in FO procedures. Another researcher investigated the preparation of a 100 nm thick $\text{Ti}_3\text{C}_2\text{T}_x$ layer on a tubular $\alpha\text{-Al}_2\text{O}_3$ support via crosslinking with the support and calcination [222]. In crossflow filtration, the membrane rejected more than 99% of VO^{2+} , had a water permeance of 11.50 LMH/bar, and was stable for 100.0 h. An anti-swelling $\text{Ti}_3\text{C}_2\text{T}_x$ MXene membrane pillared with cation-alginate was conducted by Wang et al. [223]. Because of the greater permeation rate of monovalent cations over high-valent cations, the membrane was able to select cations based on their valence. Sun et al. used thermal treatment and picked a polydopamine-modified $\alpha\text{-Al}_2\text{O}_3$ fiber as a substrate to crosslink a $\text{Ti}_3\text{C}_2\text{T}_x$ membrane with intercalated functionalized CNTs [224]. The membrane exhibited anti-swelling capability, indicating an insignificant growth in d-spacing and a dead-end system showed a great rejection rate for Rhodamine B (more than 97%). Moreover, the anti-swelling property of the membrane led to stable performance during a long period of time (50 h) in a crossflow system. In

spite of efforts to reduce the nanochannel size, the pressure-driven test failed to produce a great rate of rejection for monovalent ions. Because of the powerful driving force due to the pressure, the interactions among ions and functional groups are greatly reduced compared to concentration-driven FO [225]. Furthermore, MXene's surface functional groups facilitate ion transport and dehydration of ions [226].

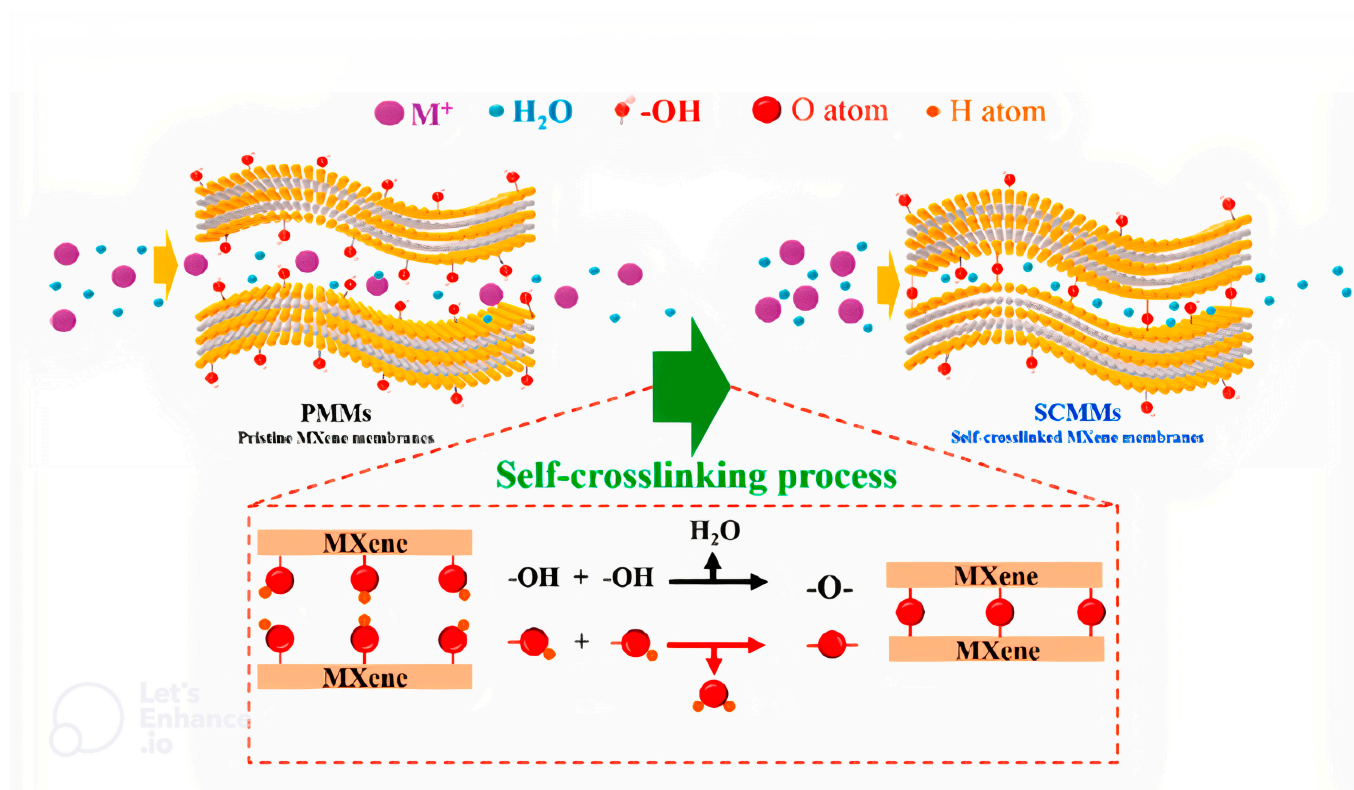


Figure 12. Structure of modified $\text{Ti}_3\text{C}_2\text{T}_x$ -based nanofiltration membranes. C: Self-crosslinked $\text{Ti}_3\text{C}_2\text{T}_x$ [221].

8.3. Composites of MXene and Polymer for High Rejection of Salt

In addition, polymeric composite membranes are known to perform better at rejecting salts than conventional membranes. Rather than acting like a selective layer, MXene enhances the polymeric membrane's efficiency in these structures. In another example, according to Wu et al., an interlayer polyamide (PA) membrane coated with $\text{Ti}_3\text{C}_2\text{T}_x$ has been developed for FO use (Figure 13) [227]. By inhibiting PA growth inside the substrate, the nanosheet affected membrane morphology, which resulted in a great water flux of 31.80 LMH and a less specific salt flux of 0.270 g/L, while 2 M sodium chloride was used as a draw solution. In situ interfacial polymerization of a $\text{Ti}_3\text{C}_2\text{T}_x$ -embedded PA membrane was conducted by Wang et al. for applications in RO (Figure 14) [228]. Because $\text{Ti}_3\text{C}_2\text{T}_x$ influenced polymer reactant diffusion through interfacial polymerization, the membrane became more hydrophilic and exhibited less surface roughness. Under 16 bar pressure, the final PA- $\text{Ti}_3\text{C}_2\text{T}_x$ membrane rejected NaCl solutions with rates of rejection of 97.90–98.50% and permeances of 2.30–2.50 LMH/bar. In another study, a surface-charged $\text{Ti}_3\text{C}_2\text{T}_x$ membrane was prepared when positively charged polyethyleneimine was deposited on $\text{Ti}_3\text{C}_2\text{T}_x$ [229]. Upon PEI deposition, the membrane developed a positive charge, which resulted in a higher rejection rate of Mg^{2+} ions and a durability of 9.0 LMH/bar under the dead-end filtration condition.

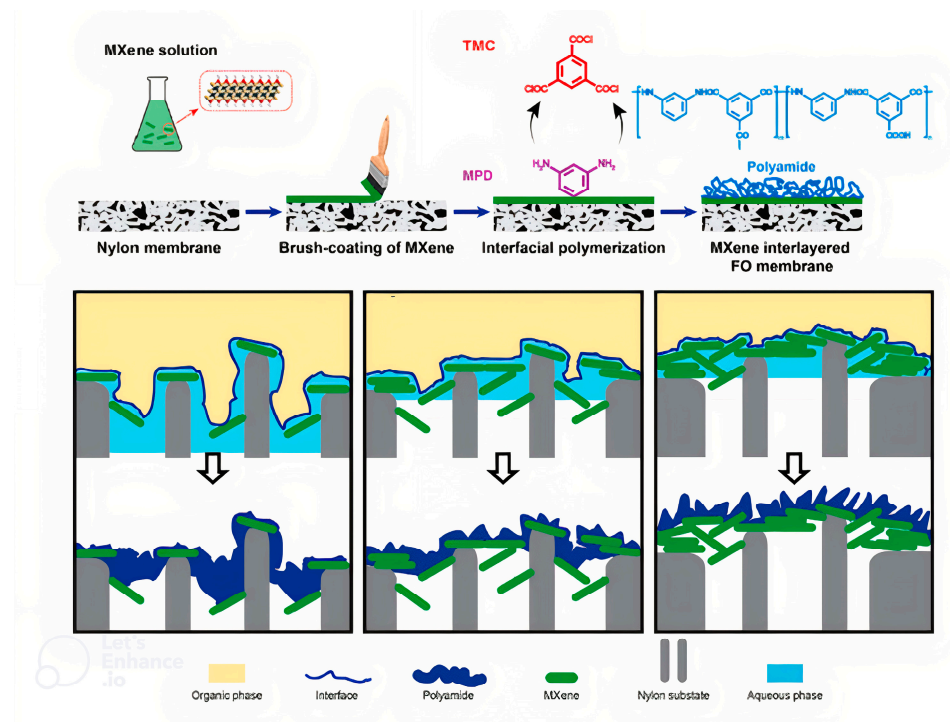


Figure 13. Polyamide membrane hybridized by $\text{Ti}_3\text{C}_2\text{T}_x$ [227].

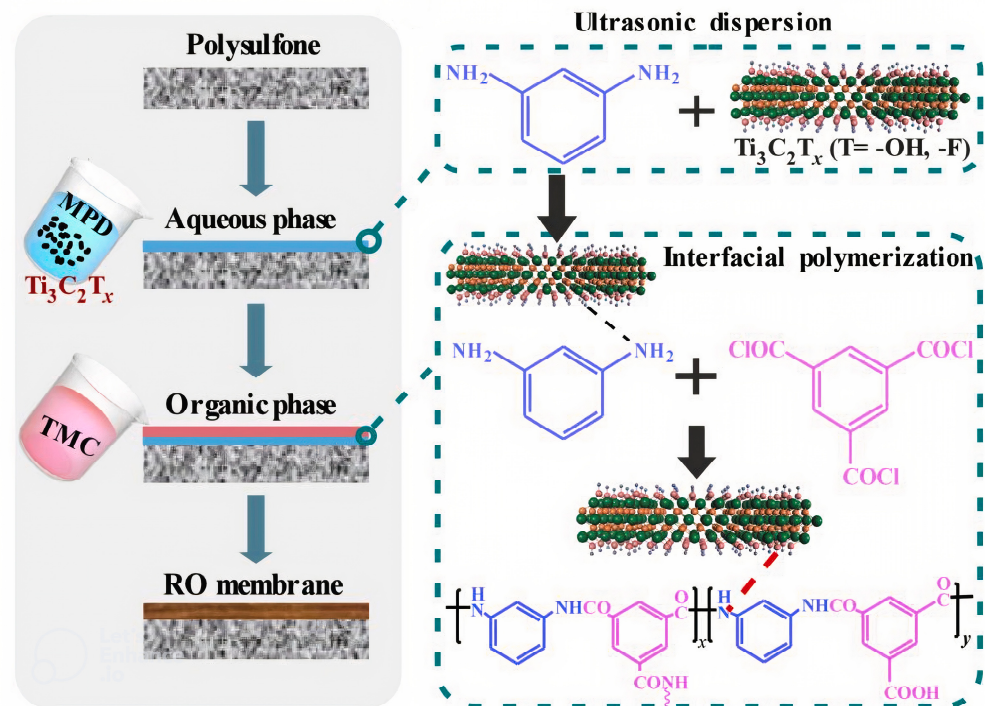


Figure 14. Synthesis of polyamide membrane [228].

8.4. MXene-Based Photothermal Membranes

Photothermally driven membrane distillation (PMD) harvest solar energy directly from the sun, making them a more cost-effective method for harvesting sunlight than PV panels due to their size, availability, fabrication, and maintenance requirements. Solar energy can be used in the photothermal membrane, and heat can be localized at the interface between air and water through the localized surface plasmon resonance (LSPR) effect. To maximize solar energy utilization, evaporators driven by solar energy should have a well-

structured design. The use of photothermal membranes has boosted water purification processes, including distillation and desalination [207–209]. The photothermal membrane comprises a photothermal layer on top and a supporting layer at the bottom. Among the most popular designs, the bilayer configuration is highly efficient in terms of photothermal utilization (solar energy absorption) as well as operability and water transfer (Figure 15).

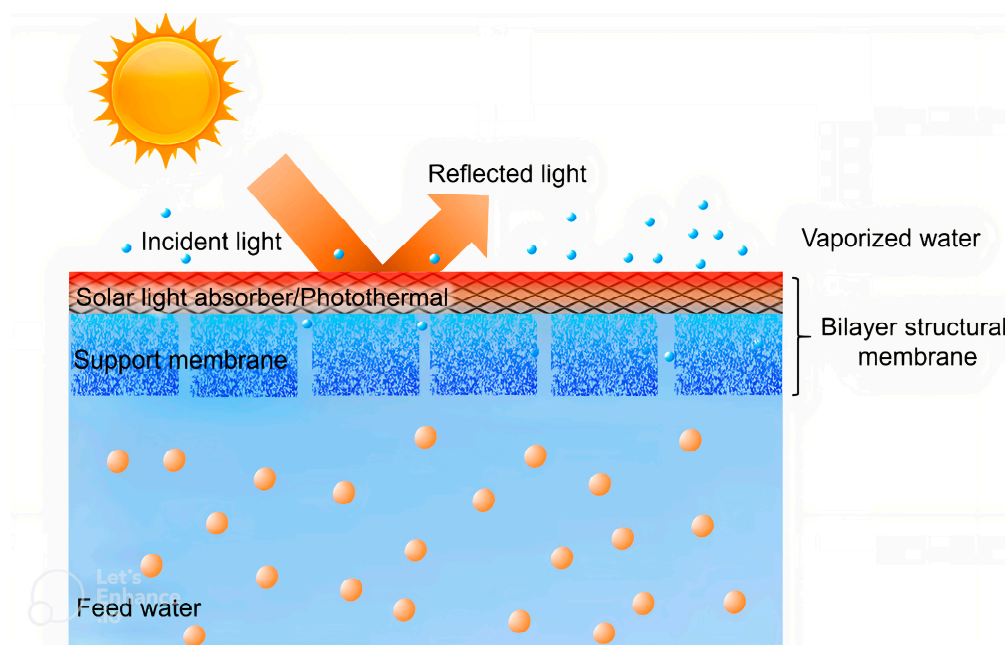


Figure 15. A photothermal membrane in general [230].

Recently, the authors of [215] have employed different photothermal materials for solar steam generation (SSG) systems [231] to manufacture PMD membranes involving carbon-based nanomaterials [232,233], inorganic semiconductors [234], polymers [235], and plasmonic materials nanostructures, such as Au, Ag, MXene, TiN, etc. [236], demonstrated intensive light absorption and strong photothermal conversion abilities [237].

MXene is known for its antifouling properties and has good light-to-heat conversion rates, making it an ideal material for photothermal membranes. Under 1 sunlight (1000 W/m^2) and various operating conditions, such as feed flow rate, and salinity, MXene-coated membranes were tested indoors with the direct contact membrane distillation (DCMD) configuration. Increasing the feed salinity and flow rate leads to a decline in water productivity. The plasmonic properties of MXene play an essential role in its high photothermal efficiency. The experiments conducted with electron energy loss spectroscopy (EELS) on MXene revealed that it displays both transversal and longitudinal surface plasmon modes ranging from visible up to 0.1 eV in the near-infrared region [238]. By incorporating MXene nanostructures into PVDF membranes, 12% less energy was consumed per unit volume of distillate. MXene's photothermal properties enhanced the membrane's anti-fouling capabilities [239].

A membrane coated with MXene with the least amount of $\text{Ti}_3\text{C}_2\text{T}_x$ achieved the highest productivity while maintaining a 65.3% photothermal efficiency [240]. Solar evaporators based on MXene demonstrate high evaporation efficiency, but their freshwater generation efficiency significantly drops when integrated with water collectors. By incorporating MXene into PMD membranes, MXene can provide optimal results regarding resource efficiency and adequate clean water [241]. As demonstrated by Chew et al. in a first proof-of-concept study of MXene in PMD, when treated with preheated saline water (65°C), the flux of the MXene-coated polyvinylidene fluoride (PVDF) membrane increased by 10% under solar irradiation versus without solar light while treating preheated saline water (65°C) [242]. Under 5.8 sunlight illumination, the PVDF membrane with MXene

coating displayed a lower flux than the PVDF membrane without MXene coating. It is due to the compact stacking structure of MXene, which dramatically increases vapor transfer resistance [243,244]. Tan et al. propose a membrane modification strategy based on emerging 2D materials with many functions. In particular, the current research aimed to assess how MXene, which has photothermal and antifouling properties, can improve direct contact membrane distillation (DCMD) performance. Uncoated and MXene-coated PVDF membranes were used for filtering bovine serum albumin (BSA) and sodium chloride (NaCl) for 21 h. Results indicate a 12% decrease in heater energy input per unit volume distillate and a 56–64% reduction in flux decline. The study demonstrated that MXene has the potential to improve the practical feasibility of membrane distillation [242].

9. MXene Nanomaterial Regeneration

Recently, research has focused on MXene's recyclability and how well it retains its properties [245,246]. Several studies have demonstrated the viability of regeneration involving hydrochloric acid [138,142,247], HNO_3 and/or $\text{Ca}(\text{NO}_3)_2$ [248,249], alcohol [250,251], NaOH [252], and thiourea [253]. For example, in a study, a removal rate of more than 90% was observed when reclaiming $\text{Ti}_3\text{C}_2\text{T}_x$ for Cs ion removal with 0.2 M HCl [246]. MX-SA_{4:20} was nearly 100% reclaimed using 8 M hydrochloric acid by Shahzad et al. [53]. Another study used 1M of HCl solution as a regenerating agent for MGMX and achieved 90% [138]. Acetate nitrate and calcium nitrate solutions were used to regenerate the absorbent material, but the findings were unsatisfactory because the first regeneration rate fell from 80% to only 47% and 33%, respectively [9,53,138,254]. According to another study, MXene/alginate has higher rates of adsorption than non-cross-linked composites due to its stability compared to calcium nitrate cross-linking [247].

10. Issues of Toxicity

Despite being considered optimistic choices for water and wastewater purification, two-dimensional MXene-based membranes, catalysts, and adsorbents must be systematically and analytically analyzed to determine their environmental impact, especially on aquatic biota and ecosystems [255]. In particular, MXenes may influence the formation of ROS due to oxidative stress [256]. To date, no comprehensive investigations were conducted to examine the probable toxic impacts of MXenes. In one case, $\text{Ti}_3\text{C}_2\text{T}_x$'s biocompatibility has been evaluated using an in vitro zebrafish embryo model, with an analysis of its potential toxicity; the aggregation patterns of $\text{Ti}_3\text{C}_2\text{T}_x$ suspensions in seawater have also been examined [255]. This result indicates that the zebrafish embryos were capable of uptaking MXenes in a dose-dependent manner; the critical poisonousness of adsorbed/attached MXenes was evaluated at different concentrations of 25, 50, 100, and 200 $\mu\text{g}/\text{mL}$. The Lethal Concentration 50 (LC50) of $\text{Ti}_3\text{C}_2\text{T}_x$ was calculated to be 257.4 g/mL according to the 96 h sigmoidal mortality curve, while the No Observed Effect Concentration (NOEC) to cause 20% death was 50 g/mL. It was determined that the lowest observed effect concentration (LOEC) ($\geq 20\%$ mortality) of $\text{Ti}_3\text{C}_2\text{T}_x$ was found to be 100 $\mu\text{g mL}^{-1}$, which resulted in a minor addition in mortality of about 21%. Additionally, there was no evidence of important teratogenic impacts on zebrafish embryos at 100 $\mu\text{g}/\text{mL}$. Based on locomotion and neurotoxicity assays, 50 g/mL of $\text{Ti}_3\text{C}_2\text{T}_x$ did not affect neuromuscular activity negatively. Hence, because the LC50 of these MXenes was more than 100 $\mu\text{g}/\text{mL}$, they were considered practically nontoxic on the basis of the Acute Toxicity Rating Scale by the Fish and Wildlife Service (FWS), allowing them to be discharged into the aquatic ecosystem at concentrations less than 100 g/mL [255]. In the early stages of the embryo, in addition to angiogenesis, MXene nanosheets were evaluated for potential toxicity. As an experimental model, 3- and 5-day incubated avian embryos were used. According to the study, 46% of MXene-exposed embryos died between 1 and 5 days after exposure, indicating that MXene could negatively affect embryogenesis. MXene also prevented the chorioallantoic membrane angiogenesis after five days of incubation at the tested concentrations. As a result of the reverse transcription polymerase chain reaction (RT-PCR) analysis of 7 genes, including

those that regulate cell survival, proliferation, cell death, and angiogenesis, MXene-treated embryos had deregulated these genes in contrast to their matched controls in the brain, heart, and liver tissues. To discover the poisonous impacts of MXenes and determine the issues of safety, several systematic and analytical research are necessary. The solubility, dispersion, long-lasting poisonousness, and biodegradation of the compounds must also be examined [257].

11. Challenges and Recommendations

Due to numerous challenges faced by researchers, the MXene-based nanomaterials study is still at an early stage despite the extensive usage of these kinds of materials in removing pollutants such as dyes, as well as organic and inorganic ions. Recent years have seen an increase in the theoretical concept for the application of MXene-based nanomaterials, but the experimental part is moving more slowly. The following are prospective suggestions for the practical utilization of nanomaterials based on MXene:

- MXenes should be investigated as an adsorbent in continuous operating systems;
- Hazardous HF is traditionally used to synthesize MXenes, which poses serious health risks. HF can be substituted with greener or less toxic chemicals to ensure an environmentally friendly MXene synthesis;
- It is necessary to study MXene-based nanomaterials' surface properties to enhance the performance of adsorption mechanisms;
- Designing an environmentally friendly and cost-effective large-scale production system for MXenes leads to opening up new avenues of commercial application for MXenes;
- For further biomedical applications, MXene-based nanomaterials must be tested for their toxicity to both the environment and humans;
- Detaching the photothermal nanoparticles from the MXene-based photothermal membranes surface is another key challenge for practical applications, which reduces the membrane's photothermal efficiency and causes secondary pollution. In this situation, chemical bonding or grafting could provide a stronger adhesive bond between the photothermal nanoparticles and the membrane surface than physical attachment.
- There are numerous applications of MXene quantum dots (MQDs) in wastewater purification, and they can be viewed as a new generation of smart nanosystems.

12. Future View on MXene

Several benefits are related to MXene, a novel group of two-dimensional materials. While MXene-based nanomaterials were studied for over ten years, they are still in the beginning stages of progress. As a promising material, MXene still requires standardization to establish durable properties such as improved biocompatibility, homogeneous dispersion, long-lasting durability, and improved productivity in comparison with other possible two-dimensional materials at the moment. In order to promote toxic removal productivity, MXene-based nanocomposite membranes, adsorbents, and electrodes should be used widely and on a large scale. This will allow cost-effective wastewater purification at home and in commercial facilities based on MBN-based products.

13. Conclusions

The development of MXenes and nanomaterial-based MXene was an excellent option for future water remediation. MXene-based nanocomposites exhibited a superior photodegradation capacity to decompose toxic environmental pollutants from water. MXene nanostructures have been a hotbed for environmental photocatalysis since they possess excellent bandgap (0.92–1.75 eV), excellent thermal and mechanical stability, perfect thermal and electrical conductivity, and high solubility in water compared to other 2D nanomaterials. In general, MXene-based composites have double the benefits in comparison to MXene alone.

A number of studies have proven that MXenes and their composites are highly effective at omitting heavy metals, dyes, and radionuclides because of their structure, which has

several properties, including a large specific surface area, greater ability to harvest light, and shorter diffusion routes for e^- and h^+ that have been photoexcited. Despite numerous challenges, these unique materials have considerable potential for improvement based on the optimistic outcomes of common studies. In the field of water and environmental remediation, there is no doubt that MXene will result in the next generation of adsorbents and catalysts.

Author Contributions: Z.P. and S.M.M. developed the idea and structure of this review article. S.A.H., A.B., Z.P., N.P.R., S.G. and S.A. wrote the manuscript, collected the materials from databases, and revised and improved the manuscript. S.M.M. and W.-H.C. supervised the manuscript. All authors have read and agreed to the published version of the manuscript.

Funding: This work is sponsored by the Ministry of Science and Technology, Taiwan (grant number: MOST 110-2628-E-011-003, MOST 109-2923-E-011-003-MY, MOST 111-NU-E-011-001-NU).

Data Availability Statement: Not applicable.

Conflicts of Interest: The authors declare no conflict of interest.

References

1. Nguyen, N.T.T.; Nguyen, L.M.; Nguyen, T.T.T.; Liew, R.K.; Nguyen, D.T.C.; Van Tran, T. Recent advances on botanical biosynthesis of nanoparticles for catalytic, water treatment and agricultural applications: A review. *Sci. Total Environ.* **2022**, *827*, 154160. [CrossRef] [PubMed]
2. Amakiri, K.T.; Canon, A.R.; Molinari, M.; Angelis-Dimakis, A. Review of oilfield produced water treatment technologies. *Chemosphere* **2022**, *298*, 134064. [CrossRef]
3. Shi, L.; Pouramini, S. Adaptive façade for building energy efficiency improvement by arithmetical optimization algorithm. *Concurr. Comput. Pract. Exp.* **2022**, *34*, e7152. [CrossRef]
4. Nayeibi, B.; Ghalebizade, M.; Niavol, K.P. Removal of Acid Red 131 by Peroxi-Coagulation Using Stainless Steel and Aluminum Electrodes: A Comparative Study. *Water Conserv. Sci. Eng.* **2021**, *6*, 201–211. [CrossRef]
5. Ruiz-Santoyo, V.; Andrade-Espinoza, B.A.; Romero-Toledo, R.; Anaya-Esparza, L.M.; Villagrán, Z.; Guerra-Contreras, A. Use of Nanostructured Photocatalysts for Dye Degradation: A Review. *Period. Polytech. Chem. Eng.* **2022**, *66*, 367–393. [CrossRef]
6. Ramalingam, G.; Nagapandiselvi, P.; Priya, A.; Rajendran, S. A review of graphene-based semiconductors for photocatalytic degradation of pollutants in wastewater. *Chemosphere* **2022**, *300*, 134391. [CrossRef]
7. Pelosato, R.; Bolognino, I.; Fontana, F.; Sora, I.N. Applications of Heterogeneous Photocatalysis to the Degradation of Oxytetracycline in Water: A Review. *Molecules* **2022**, *27*, 2743. [CrossRef]
8. Joseph, C.G.; Taufiq-Yap, Y.H.; Affandi, N.A.; Nga, J.L.H.; Vijayan, V. Photocatalytic treatment of detergent-contaminated wastewater: A short review on current progress. *Korean J. Chem. Eng.* **2022**, *39*, 484–498. [CrossRef]
9. Feng, J.; Luo, X.; Gao, M.; Abbas, A.; Xu, Y.-P.; Pouramini, S. Minimization of energy consumption by building shape optimization using an improved Manta-Ray Foraging Optimization algorithm. *Energy Rep.* **2021**, *7*, 1068–1078. [CrossRef]
10. Abdulhameed, A.S.; Jawad, A.H.; Ridwan, M.; Khadiran, T.; Wilson, L.D.; Yaseen, Z.M. Chitosan/carbon-doped TiO₂ composite for adsorption of two anionic dyes in solution and gaseous SO₂ capture: Experimental modeling and optimization. *J. Polym. Environ.* **2022**, *30*, 4619–4636. [CrossRef]
11. Jawad, A.H.; Hameed, B.; Abdulhameed, A.S. Synthesis of biohybrid magnetic chitosan-polyvinyl alcohol/MgO nanocomposite blend for remazol brilliant blue R dye adsorption: Solo and collective parametric optimization. *Polym. Bull.* **2022**, 1–21. [CrossRef]
12. Kuang, P.; Low, J.; Cheng, B.; Yu, J.; Fan, J. MXene-based photocatalysts. *J. Mater. Sci. Technol.* **2020**, *56*, 18–44. [CrossRef]
13. Jang, J.; Shahzad, A.; Woo, S.H.; Lee, D.S. Magnetic Ti₃C₂T_x (Mxene) for diclofenac degradation via the ultraviolet/chlorine advanced oxidation process. *Environ. Res.* **2020**, *182*, 108990. [CrossRef] [PubMed]
14. Bilal, M.; Mehmood, S.; Rasheed, T.; Iqbal, H.M. Antibiotics traces in the aquatic environment: Persistence and adverse environmental impact. *Curr. Opin. Environ. Sci. Health* **2020**, *13*, 68–74. [CrossRef]
15. Toth, L. *Transition Metal Carbides and Nitrides*; Elsevier: Amsterdam, The Netherlands, 2014.
16. Gogotsi, Y.G.; Andrievski, R.A. *Materials Science of Carbides, Nitrides and Borides*; Springer Science & Business Media: Berlin/Heidelberg, Germany, 2012; Volume 68.
17. Naguib, M.; Barsoum, M.W.; Gogotsi, Y. Ten years of progress in the synthesis and development of MXenes. *Adv. Mater.* **2021**, *33*, 2103393. [CrossRef]
18. Nair, S.; Gohel, J.V. A Review on Contemporary Hole Transport Materials for Perovskite Solar Cells. In *Nanotechnology for Energy and Environmental Engineering*; Springer: Cham, Switzerland, 2020; pp. 145–168. [CrossRef]
19. Jayakumar, A.; Surendranath, A.; Mohanan, P.V. 2D materials for next generation healthcare applications. *Int. J. Pharm.* **2018**, *1–2*, 309–321. [CrossRef]
20. Szuplewska, A.; Kulpińska, D.; Dybko, A.; Chudy, M.; Jastrzębska, A.M.; Olszyna, A.; Brzózka, Z. Future applications of MXenes in biotechnology, nanomedicine, and sensors. *Trends Biotechnol.* **2020**, *38*, 264–279. [CrossRef]

21. Rasool, K.; Pandey, R.P.; Rasheed, P.A.; Buczek, S.; Gogotsi, Y.; Mahmoud, K.A. Water treatment and environmental remediation applications of two-dimensional metal carbides (MXenes). *Mater. Today* **2019**, *30*, 80–102. [\[CrossRef\]](#)
22. Naguib, M.; Kurtoglu, M.; Presser, V.; Lu, J.; Niu, J.; Heon, M.; Hultman, L.; Gogotsi, Y.; Barsoum, M.W. Two-dimensional nanocrystals produced by exfoliation of Ti_3AlC_2 . *Adv. Mater.* **2011**, *23*, 4248–4253. [\[CrossRef\]](#)
23. Al-Hamadani, Y.A.; Jun, B.-M.; Yoon, M.; Taheri-Qazvini, N.; Snyder, S.A.; Jang, M.; Heo, J.; Yoon, Y. Applications of MXene-based membranes in water purification: A review. *Chemosphere* **2020**, *254*, 126821. [\[CrossRef\]](#)
24. Feng, J.; Yang, J.; Shen, Y.; Deng, W.; Chen, W.; Ma, Y.; Chen, Z.; Dong, S. Mesoporous silica nanoparticles prepared via a one-pot method for controlled release of abamectin: Properties and applications. *Microporous Mesoporous Mater.* **2021**, *311*, 110688. [\[CrossRef\]](#)
25. Khandelwal, N.; Darbha, G.K. A decade of exploring MXenes as aquatic cleaners: Covering a broad range of contaminants, current challenges and future trends. *Chemosphere* **2021**, *279*, 130587. [\[CrossRef\]](#) [\[PubMed\]](#)
26. Othman, Z.; Mackey, H.R.; Mahmoud, K.A. A critical overview of MXenes adsorption behavior toward heavy metals. *Chemosphere* **2022**, *295*, 133849. [\[CrossRef\]](#) [\[PubMed\]](#)
27. Zhu, J.; Ha, E.; Zhao, G.; Zhou, Y.; Huang, D.; Yue, G.; Hu, L.; Sun, N.; Wang, Y.; Lee, L.Y.S. Recent advance in MXenes: A promising 2D material for catalysis, sensor and chemical adsorption. *Coord. Chem. Rev.* **2017**, *352*, 306–327. [\[CrossRef\]](#)
28. Zhang, X.; Zhang, Z.; Zhou, Z. MXene-based materials for electrochemical energy storage. *J. Energy Chem.* **2018**, *27*, 73–85. [\[CrossRef\]](#)
29. Nan, J.; Guo, X.; Xiao, J.; Li, X.; Chen, W.; Wu, W.; Liu, H.; Wang, Y.; Wu, M.; Wang, G. Nanoengineering of 2D MXene-based materials for energy storage applications. *Small* **2021**, *17*, 1902085. [\[CrossRef\]](#)
30. Zhang, A.; Liu, R.; Tian, J.; Huang, W.; Liu, J. MXene-based nanocomposites for energy conversion and storage applications. *Chem.-A Eur. J.* **2020**, *26*, 6342–6359. [\[CrossRef\]](#)
31. Huang, H.; Jiang, R.; Feng, Y.; Ouyang, H.; Zhou, N.; Zhang, X.; Wei, Y. Recent development and prospects of surface modification and biomedical applications of MXenes. *Nanoscale* **2020**, *12*, 1325–1338. [\[CrossRef\]](#)
32. Ng, V.M.H.; Huang, H.; Zhou, K.; Lee, P.S.; Que, W.; Xu, Z.J.; Kong, L.B. Correction: Recent progress in layered transition metal carbides and/or nitrides (MXenes) and their composites: Synthesis and applications. *J. Mater. Chem. A* **2017**, *5*, 8769.
33. Deysher, G.; Shuck, C.E.; Hantanasirisakul, K.; Frey, N.C.; Foucher, A.C.; Maleski, K.; Sarycheva, A.; Shenoy, V.B.; Stach, E.A.; Anasori, B. Synthesis of Mo_4VAlC_4 MAX phase and two-dimensional Mo_4VC_4 MXene with five atomic layers of transition metals. *ACS Nano* **2019**, *14*, 204–217. [\[CrossRef\]](#)
34. Darvish, M.; Pouramini, M.; Bahador, H. Towards Fine-grained Image Classification with Generative Adversarial Networks and Facial Landmark Detection. In Proceedings of the 2022 International Conference on Machine Vision and Image Processing (MVIP), New York, NY, USA, 25–27 March 2022; pp. 1–6.
35. Chen, X.; Bei, G. Toughening mechanisms in nanolayered MAX phase ceramics—A review. *Materials* **2017**, *10*, 366. [\[CrossRef\]](#) [\[PubMed\]](#)
36. Yang, J.; Bao, W.; Jaumaux, P.; Zhang, S.; Wang, C.; Wang, G. MXene-based composites: Synthesis and applications in rechargeable batteries and supercapacitors. *Adv. Mater. Interfaces* **2019**, *6*, 1802004. [\[CrossRef\]](#)
37. Khazaei, M.; Ranjbar, A.; Esfarjani, K.; Bogdanovski, D.; Dronsowski, R.; Yunoki, S. Insights into exfoliation possibility of MAX phases to MXenes. *Phys. Chem. Chem. Phys.* **2018**, *20*, 8579–8592. [\[CrossRef\]](#) [\[PubMed\]](#)
38. Alhabeib, M.; Maleski, K.; Anasori, B.; Lelyukh, P.; Clark, L.; Sin, S.; Gogotsi, Y. Guidelines for synthesis and processing of two-dimensional titanium carbide ($\text{Ti}_3\text{C}_2\text{T}_x$ MXene). *Chem. Mater.* **2017**, *29*, 7633–7644. [\[CrossRef\]](#)
39. Tang, H.; Feng, H.; Wang, H.; Wan, X.; Liang, J.; Chen, Y. Highly conducting MXene–silver nanowire transparent electrodes for flexible organic solar cells. *ACS Appl. Mater. Interfaces* **2019**, *11*, 25330–25337. [\[CrossRef\]](#) [\[PubMed\]](#)
40. Xie, X.; Xue, Y.; Li, L.; Chen, S.; Nie, Y.; Ding, W.; Wei, Z. Surface Al leached Ti_3AlC_2 as a substitute for carbon for use as a catalyst support in a harsh corrosive electrochemical system. *Nanoscale* **2014**, *6*, 11035–11040. [\[CrossRef\]](#) [\[PubMed\]](#)
41. Lei, J.-C.; Zhang, X.; Zhou, Z. Recent advances in MXene: Preparation, properties, and applications. *Front. Phys.* **2015**, *10*, 276–286. [\[CrossRef\]](#)
42. Lipatov, A.; Alhabeib, M.; Lukatskaya, M.R.; Boson, A.; Gogotsi, Y.; Sinitskii, A. Effect of synthesis on quality, electronic properties and environmental stability of individual monolayer Ti_3C_2 MXene flakes. *Adv. Electron. Mater.* **2016**, *2*, 1600255. [\[CrossRef\]](#)
43. Mashtalir, O.; Naguib, M.; Mochalin, V.N.; Dall’Agnese, Y.; Heon, M.; Barsoum, M.W.; Gogotsi, Y. Intercalation and delamination of layered carbides and carbonitrides. *Nat. Commun.* **2013**, *4*, 1716. [\[CrossRef\]](#)
44. Mashtalir, O.; Lukatskaya, M.R.; Zhao, M.Q.; Barsoum, M.W.; Gogotsi, Y. Amine-assisted delamination of Nb_2C MXene for Li-ion energy storage devices. *Adv. Mater.* **2015**, *27*, 3501–3506. [\[CrossRef\]](#)
45. Naguib, M.; Gogotsi, Y. Synthesis of two-dimensional materials by selective extraction. *Acc. Chem. Res.* **2015**, *48*, 128–135. [\[CrossRef\]](#) [\[PubMed\]](#)
46. Halim, J.; Lukatskaya, M.R.; Cook, K.M.; Lu, J.; Smith, C.R.; Näslund, L.-Å.; May, S.J.; Hultman, L.; Gogotsi, Y.; Eklund, P. Transparent conductive two-dimensional titanium carbide epitaxial thin films. *Chem. Mater.* **2014**, *26*, 2374–2381. [\[CrossRef\]](#)
47. Chang, F.; Li, C.; Yang, J.; Tang, H.; Xue, M. Synthesis of a new graphene-like transition metal carbide by de-intercalating Ti_3AlC_2 . *Mater. Lett.* **2013**, *109*, 295–298. [\[CrossRef\]](#)
48. Ying, Y.; Liu, Y.; Wang, X.; Mao, Y.; Cao, W.; Hu, P.; Peng, X. Two-dimensional titanium carbide for efficiently reductive removal of highly toxic chromium (VI) from water. *ACS Appl. Mater. Interfaces* **2015**, *7*, 1795–1803. [\[CrossRef\]](#) [\[PubMed\]](#)

49. Wang, L.; Liu, D.; Lian, W.; Hu, Q.; Liu, X.; Zhou, A. The preparation of V2CT_x by facile hydrothermal-assisted etching processing and its performance in lithium-ion battery. *J. Mater. Res. Technol.* **2020**, *9*, 984–993. [\[CrossRef\]](#)
50. Sun, W.; Shah, S.; Chen, Y.; Tan, Z.; Gao, H.; Habib, T.; Radovic, M.; Green, M. Electrochemical etching of Ti₂AlC to Ti₂CT_x (MXene) in low-concentration hydrochloric acid solution. *J. Mater. Chem. A* **2017**, *5*, 21663–21668. [\[CrossRef\]](#)
51. Naguib, M.; Mochalin, V.; Barsoum, M.W.; Gogotsi, Y.G. *MXenes: A New Family of Two-Dimensional Materials—25th Anniversary Article*; Wiley: Hoboken, NJ, USA, 2014; Volume 26, pp. 992–1005.
52. Ghidui, M.; Lukatskaya, M.R.; Zhao, M.-Q.; Gogotsi, Y.; Barsoum, M.W. Conductive two-dimensional titanium carbide ‘clay’ with high volumetric capacitance. *Nature* **2014**, *516*, 78–81. [\[CrossRef\]](#)
53. Shahzad, A.; Nawaz, M.; Moztahida, M.; Jang, J.; Tahir, K.; Kim, J.; Lim, Y.; Vassiliadis, V.S.; Woo, S.H.; Lee, D.S. Ti₃C₂T_x MXene core-shell spheres for ultrahigh removal of mercuric ions. *Chem. Eng. J.* **2019**, *368*, 400–408. [\[CrossRef\]](#)
54. Zhang, P.; Wang, L.; Yuan, L.-Y.; Lan, J.-H.; Chai, Z.-F.; Shi, W.-Q. Sorption of Eu (III) on MXene-derived titanate structures: The effect of nano-confined space. *Chem. Eng. J.* **2019**, *370*, 1200–1209. [\[CrossRef\]](#)
55. Wang, X.; Garner, C.; Rochard, G.; Magne, D.; Morisset, S.; Hurand, S.; Chartier, P.; Rousseau, J.; Cabioch, T.; Coutanceau, C. A new etching environment (FeF₃/HCl) for the synthesis of two-dimensional titanium carbide MXenes: A route towards selective reactivity vs. water. *J. Mater. Chem. A* **2017**, *5*, 22012–22023. [\[CrossRef\]](#)
56. Zhang, X.; Wang, H.; Hu, R.; Huang, C.; Zhong, W.; Pan, L.; Feng, Y.; Qiu, T.; Zhang, C.J.; Yang, J. Novel solvothermal preparation and enhanced microwave absorption properties of Ti₃C₂T_x MXene modified by in situ coated Fe₃O₄ nanoparticles. *Appl. Surf. Sci.* **2019**, *484*, 383–391. [\[CrossRef\]](#)
57. Guo, J.; Peng, Q.; Fu, H.; Zou, G.; Zhang, Q. Heavy-metal adsorption behavior of two-dimensional alkalization-intercalated MXene by first-principles calculations. *J. Phys. Chem. C* **2015**, *119*, 20923–20930. [\[CrossRef\]](#)
58. Liu, G.; Shen, J.; Liu, Q.; Xiong, J.; Yang, J.; Jin, W. Ultrathin two-dimensional MXene membrane for pervaporation desalination. *J. Membr. Sci.* **2018**, *548*, 548–558. [\[CrossRef\]](#)
59. Malaki, M.; Maleki, A.; Varma, R.S. MXenes and ultrasonication. *J. Mater. Chem. A* **2019**, *7*, 10843–10857. [\[CrossRef\]](#)
60. Li, X.; Huang, Z.; Zhi, C. Environmental stability of MXenes as energy storage materials. *Front. Mater.* **2019**, *6*, 312. [\[CrossRef\]](#)
61. Maleski, K.; Mochalin, V.N.; Gogotsi, Y. Dispersions of two-dimensional titanium carbide MXene in organic solvents. *Chem. Mater.* **2017**, *29*, 1632–1640. [\[CrossRef\]](#)
62. Shah, J.B. *Synthesis of MXene-Epoxy Nanocomposites*; Drexel University: Philadelphia, PA, USA, 2017.
63. Lukatskaya, M.R.; Mashtalir, O.; Ren, C.E.; Dall’Agnese, Y.; Rozier, P.; Taberna, P.L.; Naguib, M.; Simon, P.; Barsoum, M.W.; Gogotsi, Y. Cation intercalation and high volumetric capacitance of two-dimensional titanium carbide. *Science* **2013**, *341*, 1502–1505. [\[CrossRef\]](#)
64. Ma, R.; Sasaki, T. Two-dimensional oxide and hydroxide nanosheets: Controllable high-quality exfoliation, molecular assembly, and exploration of functionality. *Acc. Chem. Res.* **2015**, *48*, 136–143. [\[CrossRef\]](#)
65. Bajraktarova-Valjakova, E.; Grozdanov, A.; Guguvcevski, L.; Korunoska-Stevkovska, V.; Kapusevska, B.; Gigovski, N.; Mijoska, A.; Bajraktarova-Misevska, C. Acid etching as surface treatment method for luting of glass-ceramic restorations, part 1: Acids, application protocol and etching effectiveness. *Open Access Maced. J. Med. Sci.* **2018**, *6*, 568. [\[CrossRef\]](#)
66. Zhu, X.; Liu, B.; Hou, H.; Huang, Z.; Zeinu, K.M.; Huang, L.; Yuan, X.; Guo, D.; Hu, J.; Yang, J. Alkaline intercalation of Ti₃C₂ MXene for simultaneous electrochemical detection of Cd (II), Pb (II), Cu (II) and Hg (II). *Electrochim. Acta* **2017**, *248*, 46–57. [\[CrossRef\]](#)
67. VahidMohammadi, A.; Kayali, E.; Orangi, J.; Beidaghi, M. Techniques for MXene delamination into single-layer flakes. In *2D Metal Carbides and Nitrides (MXenes)*; Springer: Berlin/Heidelberg, Germany, 2019; pp. 177–195.
68. Zhou, J.; Gao, S.; Guo, Z.; Sun, Z. Ti-enhanced exfoliation of V2AlC into V2C MXene for lithium-ion battery anodes. *Ceram. Int.* **2017**, *43*, 11450–11454. [\[CrossRef\]](#)
69. Xiao, J.; Wen, J.; Zhao, J.; Ma, X.; Gao, H.; Zhang, X. A safe etching route to synthesize highly crystalline Nb₂CT_x MXene for high performance asymmetric supercapacitor applications. *Electrochim. Acta* **2020**, *337*, 135803. [\[CrossRef\]](#)
70. Ghidui, M.; Naguib, M.; Shi, C.; Mashtalir, O.; Pan, L.; Zhang, B.; Yang, J.; Gogotsi, Y.; Billinge, S.J.; Barsoum, M.W. Synthesis and characterization of two-dimensional Nb₄C₃ (MXene). *Chem. Commun.* **2014**, *50*, 9517–9520. [\[CrossRef\]](#) [\[PubMed\]](#)
71. Naguib, M.; Mashtalir, O.; Carle, J.; Presser, V.; Lu, J.; Hultman, L.; Gogotsi, Y.; Barsoum, M.; Carbides, T.-D.T.M. Two-dimensional transition metal carbides. *ACS Nano* **2012**, *6*, 1322–1331. [\[CrossRef\]](#) [\[PubMed\]](#)
72. Urbankowski, P.; Anasori, B.; Makaryan, T.; Er, D.; Kota, S.; Walsh, P.L.; Zhao, M.; Shenoy, V.B.; Barsoum, M.W.; Gogotsi, Y. Synthesis of two-dimensional titanium nitride Ti₄N₃ (MXene). *Nanoscale* **2016**, *8*, 11385–11391. [\[CrossRef\]](#)
73. Meshkian, R.; Näslund, L.-Å.; Halim, J.; Lu, J.; Barsoum, M.W.; Rosen, J. Synthesis of two-dimensional molybdenum carbide, Mo₂C, from the gallium based atomic laminate Mo₂Ga₂C. *Scr. Mater.* **2015**, *108*, 147–150. [\[CrossRef\]](#)
74. Zou, D.; Lee, Y.M. Design strategy of poly (vinylidene fluoride) membranes for water treatment. *Prog. Polym. Sci.* **2022**, *128*, 101535. [\[CrossRef\]](#)
75. Fernandes, J.; Nemala, S.S.; De Bellis, G.; Capasso, A. Green Solvents for the Liquid Phase Exfoliation Production of Graphene: The Promising Case of Cyrene. *Front. Chem.* **2022**, *10*, 878799. [\[CrossRef\]](#)
76. Luo, X.-J.; Li, L.; Zhang, H.-B.; Zhao, S.; Zhang, Y.; Chen, W.; Yu, Z.-Z. Multifunctional Ti₃C₂T_x MXene/Low-Density Polyethylene Soft Robots with Programmable Configuration for Amphibious Motions. *ACS Appl. Mater. Interfaces* **2021**, *13*, 45833–45842. [\[CrossRef\]](#)

77. Liu, H.; Hu, Z.; Liu, Q.; Sun, P.; Wang, Y.; Chou, S.; Hu, Z.; Zhang, Z. Single-atom Ru anchored in nitrogen-doped MXene ($\text{Ti}_3\text{C}_2\text{Tx}$) as an efficient catalyst for the hydrogen evolution reaction at all pH values. *J. Mater. Chem. A* **2020**, *8*, 24710–24717. [\[CrossRef\]](#)
78. Kumar, J.; Soomro, R.A.; Neiber, R.R.; Ahmed, N.; Medany, S.S.; Albaqami, M.D.; Nafady, A. Ni nanoparticles embedded $\text{Ti}_3\text{C}_2\text{Tx}$ -MXene nanoarchitectures for electrochemical sensing of methylmalonic acid. *Biosensors* **2022**, *12*, 231. [\[CrossRef\]](#) [\[PubMed\]](#)
79. Zou, X.; Liu, H.; Xu, H.; Wu, X.; Han, X.; Kang, J.; Reddy, K.M. A simple approach to synthesis Cr_2CT_x MXene for efficient hydrogen evolution reaction. *Mater. Today Energy* **2021**, *20*, 100668. [\[CrossRef\]](#)
80. Vakili, M.; Cagnetta, G.; Huang, J.; Yu, G.; Yuan, J. Synthesis and regeneration of a MXene-based pollutant adsorbent by mechanochemical methods. *Molecules* **2019**, *24*, 2478. [\[CrossRef\]](#) [\[PubMed\]](#)
81. Thirumal, V.; Yuvakkumar, R.; Kumar, P.S.; Ravi, G.; Keerthana, S.; Velauthapillai, D. Facile single-step synthesis of MXene@CNTs hybrid nanocomposite by CVD method to remove hazardous pollutants. *Chemosphere* **2022**, *286*, 131733. [\[CrossRef\]](#)
82. Rasheed, T.; Rasheed, A.; Munir, S.; Ajmal, S.; Shahzad, Z.M.; Alsafari, I.A.; Ragab, S.A.; Agboola, P.O.; Shakir, I. A cost-effective approach to synthesize NiFe_2O_4 /MXene heterostructures for enhanced photodegradation performance and anti-bacterial activity. *Adv. Powder Technol.* **2021**, *32*, 2248–2257. [\[CrossRef\]](#)
83. Anasori, B.; Lukatskaya, M.R.; Gogotsi, Y. 2D metal carbides and nitrides (MXenes) for energy storage. *Nat. Rev. Mater.* **2017**, *2*, 16098. [\[CrossRef\]](#)
84. Zhang, H.; Yu, D.; Wang, W.; Gao, P.; Zhang, L.; Zhong, S.; Liu, B. Construction of a novel BON-Br-AgBr heterojunction photocatalysts as a direct Z-scheme system for efficient visible photocatalytic activity. *Appl. Surf. Sci.* **2019**, *497*, 143820. [\[CrossRef\]](#)
85. Wang, H.; Wu, Y.; Zhang, J.; Li, G.; Huang, H.; Zhang, X.; Jiang, Q. Enhancement of the electrical properties of MXene Ti_3C_2 nanosheets by post-treatments of alkalization and calcination. *Mater. Lett.* **2015**, *160*, 537–540. [\[CrossRef\]](#)
86. Wang, H.; Wu, Y.; Yuan, X.; Zeng, G.; Zhou, J.; Wang, X.; Chew, J.W. Clay-inspired MXene-based electrochemical devices and photo-electrocatalyst: State-of-the-art progresses and challenges. *Adv. Mater.* **2018**, *30*, 1704561. [\[CrossRef\]](#)
87. Kurtoglu, M.; Naguib, M.; Gogotsi, Y.; Barsoum, M.W. First principles study of two-dimensional early transition metal carbides. *MRS Commun.* **2012**, *2*, 133–137. [\[CrossRef\]](#)
88. Magnuson, M.; Halim, J.; Näsund, L.-Å. Chemical bonding in carbide MXene nanosheets. *J. Electron. Spectrosc. Relat. Phenom.* **2018**, *224*, 27–32. [\[CrossRef\]](#)
89. Jin, W.; Wu, S.; Wang, Z. Structural, electronic and mechanical properties of two-dimensional Janus transition metal carbides and nitrides. *Phys. E Low-Dimens. Syst. Nanostruct.* **2018**, *103*, 307–313. [\[CrossRef\]](#)
90. Morales-García, Á.; Fernández-Fernández, A.; Viñes, F.; Illas, F. CO_2 abatement using two-dimensional MXene carbides. *J. Mater. Chem. A* **2018**, *6*, 3381–3385. [\[CrossRef\]](#)
91. Wang, H.; Peng, R.; Hood, Z.D.; Naguib, M.; Adhikari, S.P.; Wu, Z. Titania Composites with 2D Transition Metal Carbides as Photocatalysts for Hydrogen Production under Visible-Light Irradiation. *ChemSusChem* **2016**, *9*, 1490–1497. [\[CrossRef\]](#)
92. Zhuang, Y.; Liu, Y.; Meng, X. Fabrication of TiO_2 nanofibers/MXene Ti_3C_2 nanocomposites for photocatalytic H_2 evolution by electrostatic self-assembly. *Appl. Surf. Sci.* **2019**, *496*, 143647. [\[CrossRef\]](#)
93. Ye, M.; Wang, X.; Liu, E.; Ye, J.; Wang, D. Boosting the photocatalytic activity of P25 for carbon dioxide reduction by using a surface-alkalinized titanium carbide MXene as cocatalyst. *ChemSusChem* **2018**, *11*, 1606–1611. [\[CrossRef\]](#) [\[PubMed\]](#)
94. Hantanasirisakul, K.; Zhao, M.Q.; Urbankowski, P.; Halim, J.; Anasori, B.; Kota, S.; Ren, C.E.; Barsoum, M.W.; Gogotsi, Y. Fabrication of $\text{Ti}_3\text{C}_2\text{Tx}$ MXene transparent thin films with tunable optoelectronic properties. *Adv. Electron. Mater.* **2016**, *2*, 1600050. [\[CrossRef\]](#)
95. Huang, K.; Li, Z.; Lin, J.; Han, G.; Huang, P. Correction: Two-dimensional transition metal carbides and nitrides (MXenes) for biomedical applications. *Chem. Soc. Rev.* **2018**, *47*, 6889. [\[CrossRef\]](#)
96. Dutta, A.; Basu, S.; Mukherjee, S.K.; Hossain, S.T. Wastewater treatment by microbial biofilm: A distinct possibility. In *Microbial Ecology of Wastewater Treatment Plants*; Elsevier: Amsterdam, The Netherlands, 2021; pp. 435–468.
97. Singh, J.; Yadav, P.; Pal, A.K.; Mishra, V. Water pollutants: Origin and status. In *Sensors in Water Pollutants Monitoring: Role of Material*; Springer: Berlin/Heidelberg, Germany, 2020; pp. 5–20.
98. Hosseinikhah, M.; Mokhtarani, N. Landfill leachate post-treatment by the photoelectro-peroxone process using a baffled reactor. *Sep. Purif. Technol.* **2023**, *306*, 122549. [\[CrossRef\]](#)
99. Chowdhary, P.; Raj, A.; Bharagava, R.N. Environmental pollution and health hazards from distillery wastewater and treatment approaches to combat the environmental threats: A review. *Chemosphere* **2018**, *194*, 229–246. [\[CrossRef\]](#)
100. Pouramini, Z.; Ayati, B.; Babapoor, A. Enhancing PFC ability to dye removal and power generation simultaneously via conductive spheres in the anodic chamber. *J. Electroanal. Chem.* **2022**, *917*, 116410. [\[CrossRef\]](#)
101. Crini, G.; Lichtfouse, E. Advantages and disadvantages of techniques used for wastewater treatment. *Environ. Chem. Lett.* **2019**, *17*, 145–155. [\[CrossRef\]](#)
102. Jawad, A.H.; Saber, S.E.M.; Abdulhameed, A.S.; Reghioua, A.; ALOthman, Z.A.; Wilson, L.D. Mesoporous activated carbon from mangosteen (*Garcinia mangostana*) peels by H_3PO_4 assisted microwave: Optimization, characterization, and adsorption mechanism for methylene blue dye removal. *Diam. Relat. Mater.* **2022**, *129*, 109389. [\[CrossRef\]](#)
103. Kumar, P.S.; Joshiba, G.J.; Femina, C.C.; Varshini, P.; Priyadharshini, S.; Karthick, M.; Jothirani, R. A critical review on recent developments in the low-cost adsorption of dyes from wastewater. *Desalin. Water Treat.* **2019**, *172*, 395–416. [\[CrossRef\]](#)

104. Pouramini, Z.; Mousavi, S.M.; Babapoor, A.; Hashemi, S.A.; Lai, C.W.; Mazaheri, Y.; Chiang, W.-H. Effect of Metal Atom in Zeolitic Imidazolate Frameworks (ZIF-8 & 67) for Removal of Dyes and Antibiotics from Wastewater: A Review. *Catalysts* **2023**, *13*, 155.
105. Jawad, A.H.; Rangabhashiyam, S.; Abdulhameed, A.S.; Syed-Hassan, S.S.A.; ALOthman, Z.A.; Wilson, L.D. Process optimization and adsorptive mechanism for reactive blue 19 dye by magnetic crosslinked chitosan/MgO/Fe₃O₄ biocomposite. *J. Polym. Environ.* **2022**, *30*, 2759–2773. [\[CrossRef\]](#)
106. TaheriAshtiani, N.; Ayati, B. Using chitosan-based heterogeneous catalyst for degradation of Acid Blue 25 in the effective electro-Fenton process with rotating cathodes. *J. Electroanal. Chem.* **2022**, *905*, 115983. [\[CrossRef\]](#)
107. Nayebe, B.; Niyavol, K.P.; Nayebe, B.; Kim, S.Y.; Nam, K.T.; Jang, H.W.; Varma, R.S.; Shokouhimehr, M. Prussian blue-based nanostructured materials: Catalytic applications for environmental remediation and energy conversion. *Mol. Catal.* **2021**, *514*, 111835. [\[CrossRef\]](#)
108. Saravanan, A.; Kumar, P.S.; Jeevanantham, S.; Karishma, S.; Tajsabreen, B.; Yaashikaa, P.; Reshma, B. Effective water/wastewater treatment methodologies for toxic pollutants removal: Processes and applications towards sustainable development. *Chemosphere* **2021**, *280*, 130595. [\[CrossRef\]](#)
109. Pouramini, Z. The VOCs catalytic combustion by perovskite catalysts: A mini-review. *Adv. Appl. NanoBio-Technol.* **2022**, *3*, 23–30.
110. Amini, Z.P. Using nanomembrane to heavy metal removal from wastewater: A mini-review. *Adv. Appl. NanoBio-Technol.* **2022**, *3*, 7–13.
111. Wang, D.; Guo, F.; Wu, Y.; Li, Z.; Wu, G. Technical, economic and environmental assessment of coagulation/filtration tertiary treatment processes in full-scale wastewater treatment plants. *J. Clean. Prod.* **2018**, *170*, 1185–1194. [\[CrossRef\]](#)
112. Nidheesh, P.; Scaria, J.; Babu, D.S.; Kumar, M.S. An overview on combined electrocoagulation-degradation processes for the effective treatment of water and wastewater. *Chemosphere* **2021**, *263*, 127907. [\[CrossRef\]](#) [\[PubMed\]](#)
113. Paździor, K.; Bilińska, L.; Ledakowicz, S. A review of the existing and emerging technologies in the combination of AOPs and biological processes in industrial textile wastewater treatment. *Chem. Eng. J.* **2019**, *376*, 120597. [\[CrossRef\]](#)
114. Zhao, C.; Dong, Y.; Feng, Y.; Li, Y.; Dong, Y. Thermal desorption for remediation of contaminated soil: A review. *Chemosphere* **2019**, *221*, 841–855. [\[CrossRef\]](#)
115. Guo, Z.; Sun, Y.; Pan, S.-Y.; Chiang, P.-C. Integration of green energy and advanced energy-efficient technologies for municipal wastewater treatment plants. *Int. J. Environ. Res. Public Health* **2019**, *16*, 1282. [\[CrossRef\]](#)
116. Udaiyappan, A.F.M.; Hasan, H.A.; Takriff, M.S.; Abdullah, S.R.S. A review of the potentials, challenges and current status of microalgae biomass applications in industrial wastewater treatment. *J. Water Process Eng.* **2017**, *20*, 8–21. [\[CrossRef\]](#)
117. Nanda, S.; Berruti, F. Municipal solid waste management and landfilling technologies: A review. *Environ. Chem. Lett.* **2021**, *19*, 1433–1456. [\[CrossRef\]](#)
118. Karimi-Maleh, H.; Kumar, B.G.; Rajendran, S.; Qin, J.; Vadivel, S.; Durgalakshmi, D.; Gracia, F.; Soto-Moscoco, M.; Orooji, Y.; Karimi, F. Tuning of metal oxides photocatalytic performance using Ag nanoparticles integration. *J. Mol. Liq.* **2020**, *314*, 113588. [\[CrossRef\]](#)
119. Jawad, A.H.; Abdulhameed, A.S.; Selvasembian, R.; ALOthman, Z.A.; Wilson, L.D. Magnetic biohybrid chitosan-ethylene glycol diglycidyl ether/magnesium oxide/Fe₃O₄ nanocomposite for textile dye removal: Box–Behnken design optimization and mechanism study. *J. Polym. Res.* **2022**, *29*, 207. [\[CrossRef\]](#)
120. Baby, R.; Saifullah, B.; Hussein, M.Z. Carbon nanomaterials for the treatment of heavy metal-contaminated water and environmental remediation. *Nanoscale Res. Lett.* **2019**, *14*, 341. [\[CrossRef\]](#)
121. Lu, Y.C.; Mao, J.H.; Zhang, W.; Wang, C.; Cao, M.; Wang, X.D.; Wang, K.Y.; Xiong, X.H. A novel strategy for selective removal and rapid collection of triclosan from aquatic environment using magnetic molecularly imprinted nano– polymers. *Chemosphere* **2020**, *238*, 124640. [\[CrossRef\]](#)
122. Lakouraj, M.M.; Mojerlou, F.; Zare, E.N. Nanogel and superparamagnetic nanocomposite based on sodium alginate for sorption of heavy metal ions. *Carbohydr. Polym.* **2014**, *106*, 34–41. [\[CrossRef\]](#)
123. El-Naggar, M.E.; Radwan, E.K.; El-Wakeel, S.T.; Kafafy, H.; Gad-Allah, T.A.; El-Kalliny, A.S.; Shaheen, T.I. Synthesis, characterization and adsorption properties of microcrystalline cellulose based nanogel for dyes and heavy metals removal. *Int. J. Biol. Macromol.* **2018**, *113*, 248–258. [\[CrossRef\]](#)
124. Zain, Z.M.; Abdulhameed, A.S.; Jawad, A.H.; ALOthman, Z.A.; Yaseen, Z.M. A pH-sensitive surface of chitosan/sepiolite clay/algae biocomposite for the removal of malachite green and remazol brilliant blue R dyes: Optimization and adsorption mechanism study. *J. Polym. Environ.* **2023**, *31*, 501–518. [\[CrossRef\]](#)
125. Abdulhameed, A.S.; Jawad, A.H.; Kashi, E.; Radzun, K.A.; ALOthman, Z.A.; Wilson, L.D. Insight into adsorption mechanism, modeling, and desirability function of crystal violet and methylene blue dyes by microalgae: Box-Behnken design application. *Algal Res.* **2022**, *67*, 102864. [\[CrossRef\]](#)
126. Razali, N.S.; Abdulhameed, A.S.; Jawad, A.H.; ALOthman, Z.A.; Yousef, T.A.; Al-Duaij, O.K.; Alsaiani, N.S. High-surface-area-activated carbon derived from mango peels and seeds wastes via microwave-induced ZnCl₂ activation for adsorption of methylene blue dye molecules: Statistical optimization and mechanism. *Molecules* **2022**, *27*, 6947. [\[CrossRef\]](#) [\[PubMed\]](#)
127. Jani, N.A.; Haddad, L.; Abdulhameed, A.S.; Jawad, A.H.; ALOthman, Z.A.; Yaseen, Z.M. Modeling and optimization of the adsorptive removal of crystal violet dye by durian (*Durio zibethinus*) seeds powder: Insight into kinetic, isotherm, thermodynamic, and adsorption mechanism. *Biomass Convers. Biorefin.* **2022**, 1–14. [\[CrossRef\]](#)

128. Suhaimi, A.; Abdulhameed, A.S.; Jawad, A.H.; Yousef, T.A.; Al Duaij, O.; AlOthman, Z.A.; Wilson, L.D. Production of large surface area activated carbon from a mixture of carrot juice pulp and pomegranate peel using microwave radiation-assisted ZnCl_2 activation: An optimized removal process and tailored adsorption mechanism of crystal violet dye. *Diam. Relat. Mater.* **2022**, *130*, 109456. [\[CrossRef\]](#)
129. Schultz, T.; Frey, N.C.; Hantanasirisakul, K.; Park, S.; May, S.J.; Shenoy, V.B.; Gogotsi, Y.; Koch, N. Surface termination dependent work function and electronic properties of $\text{Ti}_3\text{C}_2\text{T}_x$ MXene. *Chem. Mater.* **2019**, *31*, 6590–6597. [\[CrossRef\]](#)
130. Tunesi, M.M.; Soomro, R.A.; Han, X.; Zhu, Q.; Wei, Y.; Xu, B. Application of MXenes in environmental remediation technologies. *Nano Converg.* **2021**, *8*, 5. [\[CrossRef\]](#)
131. Ibrahim, Y.; Kassab, A.; Eid, K.M.; Abdullah, A.; Ozoemena, K.I.; Elzatahry, A. Unveiling fabrication and environmental remediation of MXene-based nanoarchitectures in toxic metals removal from wastewater: Strategy and mechanism. *Nanomaterials* **2020**, *10*, 885. [\[CrossRef\]](#)
132. Velusamy, K.; Chellam, P.; Kumar, P.S.; Venkatachalam, J.; Periyasamy, S.; Saravanan, R. Functionalization of MXene-based nanomaterials for the treatment of micropollutants in aquatic system: A review. *Environ. Pollut.* **2022**, *301*, 119034. [\[CrossRef\]](#)
133. Dong, Y.; Sang, D.; He, C.; Sheng, X.; Lei, L. Mxene/alginate composites for lead and copper ion removal from aqueous solutions. *RSC Adv.* **2019**, *9*, 29015–29022. [\[CrossRef\]](#) [\[PubMed\]](#)
134. Jin, L.; Chai, L.; Yang, W.; Wang, H.; Zhang, L. Two-dimensional titanium carbides ($\text{Ti}_3\text{C}_2\text{T}_x$) functionalized by poly (m-phenylenediamine) for efficient adsorption and reduction of hexavalent chromium. *Int. J. Environ. Res. Public Health* **2020**, *17*, 167. [\[CrossRef\]](#) [\[PubMed\]](#)
135. Zou, G.; Guo, J.; Peng, Q.; Zhou, A.; Zhang, Q.; Liu, B. Synthesis of urchin-like rutile titania carbon nanocomposites by iron-facilitated phase transformation of MXene for environmental remediation. *J. Mater. Chem. A* **2016**, *4*, 489–499. [\[CrossRef\]](#)
136. Karthikeyan, P.; Ramkumar, K.; Pandi, K.; Fayyaz, A.; Meenakshi, S.; Park, C.M. Effective removal of Cr (VI) and methyl orange from the aqueous environment using two-dimensional (2D) $\text{Ti}_3\text{C}_2\text{T}_x$ MXene nanosheets. *Ceram. Int.* **2021**, *47*, 3692–3698. [\[CrossRef\]](#)
137. Krstić, V.; Urošević, T.; Pešovski, B. A review on adsorbents for treatment of water and wastewaters containing copper ions. *Chem. Eng. Sci.* **2018**, *192*, 273–287. [\[CrossRef\]](#)
138. Shahzad, A.; Rasool, K.; Miran, W.; Nawaz, M.; Jang, J.; Mahmoud, K.A.; Lee, D.S. Mercuric ion capturing by recoverable titanium carbide magnetic nanocomposite. *J. Hazard. Mater.* **2018**, *344*, 811–818. [\[CrossRef\]](#) [\[PubMed\]](#)
139. Shahzad, A.; Rasool, K.; Miran, W.; Nawaz, M.; Jang, J.; Mahmoud, K.A.; Lee, D.S. Two-dimensional $\text{Ti}_3\text{C}_2\text{T}_x$ MXene nanosheets for efficient copper removal from water. *ACS Sustain. Chem. Eng.* **2017**, *5*, 11481–11488. [\[CrossRef\]](#)
140. Elumalai, S.; Yoshimura, M.; Ogawa, M. Simultaneous delamination and rutile formation on the surface of $\text{Ti}_3\text{C}_2\text{T}_x$ MXene for copper adsorption. *Chem.-Asian J.* **2020**, *15*, 1044–1051. [\[CrossRef\]](#) [\[PubMed\]](#)
141. Gan, D.; Huang, Q.; Dou, J.; Huang, H.; Chen, J.; Liu, M.; Wen, Y.; Yang, Z.; Zhang, X.; Wei, Y. Bioinspired functionalization of MXenes ($\text{Ti}_3\text{C}_2\text{T}_x$) with amino acids for efficient removal of heavy metal ions. *Appl. Surf. Sci.* **2020**, *504*, 144603. [\[CrossRef\]](#)
142. Shahzad, A.; Jang, J.; Lim, S.-R.; Lee, D.S. Unique selectivity and rapid uptake of molybdenum-disulfide-functionalized MXene nanocomposite for mercury adsorption. *Environ. Res.* **2020**, *182*, 109005. [\[CrossRef\]](#) [\[PubMed\]](#)
143. Fu, K.; Liu, X.; Yu, D.; Luo, J.; Wang, Z.; Crittenden, J.C. Highly efficient and selective Hg (II) removal from water using multilayered $\text{Ti}_3\text{C}_2\text{O}_x$ MXene via adsorption coupled with catalytic reduction mechanism. *Environ. Sci. Technol.* **2020**, *54*, 16212–16220. [\[CrossRef\]](#) [\[PubMed\]](#)
144. Wu, Y.; Chen, H.; Xiao, J.; Liu, D.; Liu, Z.; Qian, Y.; Xi, H. Adsorptive Separation of Methanol–Acetone on Isostructural Series of Metal–Organic Frameworks M-BTC (M = Ti, Fe, Cu, Co, Ru, Mo): A Computational Study of Adsorption Mechanisms and Metal-Substitution Impacts. *ACS Appl. Mater. Interfaces* **2015**, *7*, 26930–26940. [\[CrossRef\]](#) [\[PubMed\]](#)
145. Wang, S.; Liu, Y.; Lü, Q.-F.; Zhuang, H. Facile preparation of biosurfactant-functionalized Ti_2CTx MXene nanosheets with an enhanced adsorption performance for Pb (II) ions. *J. Mol. Liq.* **2020**, *297*, 111810. [\[CrossRef\]](#)
146. Luo, S.; Wang, R.; Yin, J.; Jiao, T.; Chen, K.; Zou, G.; Zhang, L.; Zhou, J.; Zhang, L.; Peng, Q. Preparation and dye degradation performances of self-assembled MXene- Co_3O_4 nanocomposites synthesized via solvothermal approach. *ACS Omega* **2019**, *4*, 3946–3953. [\[CrossRef\]](#)
147. Li, K.; Zou, G.; Jiao, T.; Xing, R.; Zhang, L.; Zhou, J.; Zhang, Q.; Peng, Q. Self-assembled MXene-based nanocomposites via layer-by-layer strategy for elevated adsorption capacities. *Colloids Surf. A Physicochem. Eng. Asp.* **2018**, *553*, 105–113. [\[CrossRef\]](#)
148. Mashtalir, O.; Cook, K.M.; Mochalin, V.N.; Crowe, M.; Barsoum, M.W.; Gogotsi, Y. Dye adsorption and decomposition on two-dimensional titanium carbide in aqueous media. *J. Mater. Chem. A* **2014**, *2*, 14334–14338. [\[CrossRef\]](#)
149. Gao, Y.; Wang, L.; Zhou, A.; Li, Z.; Chen, J.; Bala, H.; Hu, Q.; Cao, X. Hydrothermal synthesis of $\text{TiO}_2/\text{Ti}_3\text{C}_2$ nanocomposites with enhanced photocatalytic activity. *Mater. Lett.* **2015**, *150*, 62–64. [\[CrossRef\]](#)
150. Peng, C.; Wei, P.; Chen, X.; Zhang, Y.; Zhu, F.; Cao, Y.; Wang, H.; Yu, H.; Peng, F. A hydrothermal etching route to synthesis of 2D MXene (Ti_3C_2 , Nb_2C): Enhanced exfoliation and improved adsorption performance. *Ceram. Int.* **2018**, *44*, 18886–18893. [\[CrossRef\]](#)
151. Yao, C.; Zhang, W.; Xu, L.; Cheng, M.; Su, Y.; Xue, J.; Liu, J.; Hou, S. A facile synthesis of porous MXene-based freestanding film and its spectacular electrosorption performance for organic dyes. *Sep. Purif. Technol.* **2021**, *263*, 118365. [\[CrossRef\]](#)
152. Cai, C.; Wang, R.; Liu, S.; Yan, X.; Zhang, L.; Wang, M.; Tong, Q.; Jiao, T. Synthesis of self-assembled phytic acid-MXene nanocomposites via a facile hydrothermal approach with elevated dye adsorption capacities. *Colloids Surf. A Physicochem. Eng. Asp.* **2020**, *589*, 124468. [\[CrossRef\]](#)

153. Kim, S.; Gholamirad, F.; Yu, M.; Park, C.M.; Jang, A.; Jang, M.; Taheri-Qazvini, N.; Yoon, Y. Enhanced adsorption performance for selected pharmaceutical compounds by sonicated $\text{Ti}_3\text{C}_2\text{T}_x$ MXene. *Chem. Eng. J.* **2021**, *406*, 126789. [\[CrossRef\]](#)
154. Zhang, P.; Xiang, M.; Liu, H.; Yang, C.; Deng, S. Novel two-dimensional magnetic titanium carbide for methylene blue removal over a wide pH range: Insight into removal performance and mechanism. *ACS Appl. Mater. Interfaces* **2019**, *11*, 24027–24036. [\[CrossRef\]](#)
155. da Silva, M.P.; de Souza, A.C.A.; de Lima Ferreira, L.E.; Neto, L.M.P.; Nascimento, B.F.; de Araújo, C.M.B.; Fraga, T.J.M.; da Motta Sobrinho, M.A.; Ghislandi, M.G. Photodegradation of Reactive Black 5 and raw textile wastewater by heterogeneous photo-Fenton reaction using amino- Fe_3O_4 -functionalized graphene oxide as nanocatalyst. *Environ. Adv.* **2021**, *4*, 100064. [\[CrossRef\]](#)
156. Li, Q.; Hu, B.; Yang, Q.; Cai, X.; Nie, M.; Jin, Y.; Zhou, L.; Xu, Y.; Pan, Q.; Fang, L. Interaction mechanism between multi-layered MoS_2 and H_2O_2 for self-generation of reactive oxygen species. *Environ. Res.* **2020**, *191*, 110227. [\[CrossRef\]](#)
157. Tan, C.; Cheng, X.; Xu, T.; Chen, K.; Xiang, H.; Su, L. Crystalline boron significantly accelerates Fe (III)/PMS reaction as an electron donor: Iron recycling, reactive species generation, and acute toxicity evaluation. *Chem. Eng. J.* **2023**, *452*, 139154. [\[CrossRef\]](#)
158. Nayebi, B.; Ayati, B. Degradation of emerging amoxicillin compound from water using the electro-Fenton process with an aluminum anode. *Water Conserv. Sci. Eng.* **2021**, *6*, 45–54. [\[CrossRef\]](#)
159. Cui, Y.; Zhang, D.; Shen, K.; Nie, S.; Liu, M.; Huang, H.; Deng, F.; Zhou, N.; Zhang, X.; Wei, Y. Biomimetic anchoring of Fe_3O_4 onto Ti_3C_2 MXene for highly efficient removal of organic dyes by Fenton reaction. *J. Environ. Chem. Eng.* **2020**, *8*, 104369. [\[CrossRef\]](#)
160. Wan, Z.; Wang, J. Ce-Fe-reduced graphene oxide nanocomposite as an efficient catalyst for sulfamethazine degradation in aqueous solution. *Environ. Sci. Pollut. Res.* **2016**, *23*, 18542–18551. [\[CrossRef\]](#) [\[PubMed\]](#)
161. Cui, Y.; Liu, M.; Huang, H.; Zhang, D.; Chen, J.; Mao, L.; Zhou, N.; Deng, F.; Zhang, X.; Wei, Y. A novel one-step strategy for preparation of Fe_3O_4 -loaded Ti_3C_2 MXenes with high efficiency for removal organic dyes. *Ceram. Int.* **2020**, *46*, 11593–11601. [\[CrossRef\]](#)
162. He, L.; Huang, D.; He, Z.; Yang, X.; Yue, G.; Zhu, J.; Astruc, D.; Zhao, P. Nanoscale zero-valent iron intercalated 2D titanium carbides for removal of Cr (VI) in aqueous solution and the mechanistic aspect. *J. Hazard. Mater.* **2020**, *388*, 121761. [\[CrossRef\]](#) [\[PubMed\]](#)
163. Shi, W.; Fu, Y.; Hao, C.; Guo, F.; Tang, Y. Heterogeneous photo-Fenton process over magnetically recoverable MnFe_2O_4 /MXene hierarchical heterostructure for boosted degradation of tetracycline. *Mater. Today Commun.* **2022**, *33*, 104449. [\[CrossRef\]](#)
164. Ma, Y.; Lv, X.; Xiong, D.; Zhao, X.; Zhang, Z. Catalytic degradation of ranitidine using novel magnetic Ti_3C_2 -based MXene nanosheets modified with nanoscale zero-valent iron particles. *Appl. Catal. B Environ.* **2021**, *284*, 119720. [\[CrossRef\]](#)
165. Wang, C.; Ye, J.; Liang, L.; Cui, X.; Kong, L.; Li, N.; Cheng, Z.; Peng, W.; Yan, B.; Chen, G. Application of MXene-based materials in Fenton-like systems for organic wastewater treatment: A review. *Sci. Total Environ.* **2022**, *862*, 160539. [\[CrossRef\]](#)
166. Li, N.; Wang, Y.; Cheng, X.; Dai, H.; Yan, B.; Chen, G.; Wang, S. Influences and mechanisms of phosphate ions onto persulfate activation and organic degradation in water treatment: A review. *Water Res.* **2022**, *222*, 118896. [\[CrossRef\]](#)
167. Devi, P.; Das, U.; Dalai, A.K. In-situ chemical oxidation: Principle and applications of peroxide and persulfate treatments in wastewater systems. *Sci. Total Environ.* **2016**, *571*, 643–657. [\[CrossRef\]](#) [\[PubMed\]](#)
168. Peng, W.; Dong, Y.; Fu, Y.; Wang, L.; Li, Q.; Liu, Y.; Fan, Q.; Wang, Z. Non-radical reactions in persulfate-based homogeneous degradation processes: A review. *Chem. Eng. J.* **2021**, *421*, 127818. [\[CrossRef\]](#)
169. Yan, X.; Yue, D.; Guo, C.; Wang, S.; Qian, X.; Zhao, Y. Effective removal of chlorinated organic pollutants by bimetallic iron-nickel sulfide activation of peroxydisulfate. *Chin. Chem. Lett.* **2020**, *31*, 1535–1539. [\[CrossRef\]](#)
170. Hu, L.; Xiao, R.; Wang, X.; Wang, X.; Wang, C.; Wen, J.; Gu, W.; Zhu, C. MXene-induced electronic optimization of metal-organic framework-derived CoFe LDH nanosheet arrays for efficient oxygen evolution. *Appl. Catal. B Environ.* **2021**, *298*, 120599. [\[CrossRef\]](#)
171. Li, S.; Gu, M.; Huang, J.; Wang, Y.; Yu, G. Oligolayered Co@MXene with a $\text{Co}\cdots\text{SO}_3$ cation- π bridge for ultra-rapid catalytic oxidation of a novel “forever chemical” OBS. *Appl. Catal. B Environ.* **2022**, *311*, 121364. [\[CrossRef\]](#)
172. Song, H.; Zu, D.; Li, C.; Zhou, R.; Wang, Y.; Zhang, W.; Pan, S.; Cai, Y.; Li, Z.; Shen, Y. Ultrafast activation of peroxymonosulfate by reduction of trace Fe^{3+} with Ti_3C_2 MXene under neutral and alkaline conditions: Reducibility and confinement effect. *Chem. Eng. J.* **2021**, *423*, 130012. [\[CrossRef\]](#)
173. Song, X.; Wang, H.; Jin, S.; Lv, M.; Zhang, Y.; Kong, X.; Xu, H.; Ma, T.; Luo, X.; Tan, H. Oligolayered $\text{Ti}_3\text{C}_2\text{T}_x$ MXene towards high performance lithium/sodium storage. *Nano Res.* **2020**, *13*, 1659–1667. [\[CrossRef\]](#)
174. Jin, L.; You, S.; Yao, Y.; Chen, H.; Wang, Y.; Liu, Y. An electroactive single-atom copper anchored MXene nanohybrid filter for ultrafast water decontamination. *J. Mater. Chem. A* **2021**, *9*, 25964–25973. [\[CrossRef\]](#)
175. Ma, Y.; Xiong, D.; Lv, X.; Zhao, X.; Meng, C.; Xie, H.; Zhang, Z. Rapid and long-lasting acceleration of zero-valent iron nanoparticles/ Ti_3C_2 -based MXene/peroxymonosulfate oxidation with bi-active centers toward ranitidine removal. *J. Mater. Chem. A* **2021**, *9*, 19817–19833. [\[CrossRef\]](#)
176. Cai, T.; Wang, L.; Liu, Y.; Zhang, S.; Dong, W.; Chen, H.; Yi, X.; Yuan, J.; Xia, X.; Liu, C. Ag_3PO_4 / Ti_3C_2 MXene interface materials as a Schottky catalyst with enhanced photocatalytic activities and anti-photocorrosion performance. *Appl. Catal. B Environ.* **2018**, *239*, 545–554. [\[CrossRef\]](#)
177. Fayyaz, A.; Saravanakumar, K.; Talukdar, K.; Kim, Y.; Yoon, Y.; Park, C.M. Catalytic oxidation of naproxen in cobalt spinel ferrite decorated $\text{Ti}_3\text{C}_2\text{T}_x$ MXene activated persulfate system: Mechanisms and pathways. *Chem. Eng. J.* **2021**, *407*, 127842. [\[CrossRef\]](#)

178. Ding, M.; Chen, W.; Xu, H.; Lu, C.; Lin, T.; Shen, Z.; Tao, H.; Zhang, K. Synergistic Features of Superoxide Molecule Anchoring and Charge Transfer on Two-Dimensional $\text{Ti}_3\text{C}_2\text{Tx}$ MXene for Efficient Peroxymonosulfate Activation. *ACS Appl. Mater. Interfaces* **2020**, *12*, 9209–9218. [\[CrossRef\]](#)
179. Yang, P.; Li, S.; Xiaofu, L.; Xiaojing, A.; Liu, D.; Huang, W. Singlet oxygen-dominated activation of peroxymonosulfate by CuO/MXene nanocomposites for efficient decontamination of carbamazepine under high salinity conditions: Performance and singlet oxygen evolution mechanism. *Sep. Purif. Technol.* **2022**, *285*, 120288. [\[CrossRef\]](#)
180. Song, H.; Pan, S.; Wang, Y.; Cai, Y.; Zhang, W.; Shen, Y.; Li, C. MXene-mediated electron transfer in $\text{Cu (II)}/\text{PMS}$ process: From Cu (III) to Cu (I) . *Sep. Purif. Technol.* **2022**, *12*, 121428. [\[CrossRef\]](#)
181. Zeng, H.; Deng, L.; Yang, L.; Wu, H.; Zhang, H.; Zhou, C.; Liu, B.; Shi, Z. Novel Prussian blue analogues@MXene nanocomposite as heterogeneous activator of peroxymonosulfate for the degradation of coumarin: The nonnegligible role of Lewis-acid sites on MXene. *Chem. Eng. J.* **2021**, *416*, 128071. [\[CrossRef\]](#)
182. Zheng, H.; Bao, J.; Huang, Y.; Xiang, L.; Ren, B.; Du, J.; Nadagouda, M.N.; Dionysiou, D.D. Efficient degradation of atrazine with porous sulfurized Fe_2O_3 as catalyst for peroxymonosulfate activation. *Appl. Catal. B Environ.* **2019**, *259*, 118056. [\[CrossRef\]](#)
183. Chen, G.; Nengzi, L.-C.; Gao, Y.; Zhu, G.; Gou, J.; Cheng, X. Degradation of tartrazine by peroxymonosulfate through magnetic $\text{Fe}_2\text{O}_3/\text{Mn}_2\text{O}_3$ composites activation. *Chin. Chem. Lett.* **2020**, *31*, 2730–2736. [\[CrossRef\]](#)
184. Yun, E.-T.; Yoo, H.-Y.; Bae, H.; Kim, H.-I.; Lee, J. Exploring the role of persulfate in the activation process: Radical precursor versus electron acceptor. *Environ. Sci. Technol.* **2017**, *51*, 10090–10099. [\[CrossRef\]](#)
185. Zhan, X.; Si, C.; Zhou, J.; Sun, Z. MXene and MXene-based composites: Synthesis, properties and environment-related applications. *Nanoscale Horiz.* **2020**, *5*, 235–258. [\[CrossRef\]](#)
186. Hojjati-Najafabadi, A.; Mansoorianfar, M.; Liang, T.; Shahin, K.; Wen, Y.; Bahrami, A.; Karaman, C.; Zare, N.; Karimi-Maleh, H.; Vasseghian, Y. Magnetic-MXene-based nanocomposites for water and wastewater treatment: A review. *J. Water Process Eng.* **2022**, *47*, 102696. [\[CrossRef\]](#)
187. Sharma, S.K.; Kumar, A.; Sharma, G.; Vo, D.-V.N.; García-Peñas, A.; Moradi, O.; Sillanpää, M. MXenes based nano-heterojunctions and composites for advanced photocatalytic environmental detoxification and energy conversion: A review. *Chemosphere* **2021**, *291*, 132923. [\[CrossRef\]](#) [\[PubMed\]](#)
188. Javaid, A.; Latif, S.; Imran, M.; Hussain, N.; Bilal, M.; Iqbal, H.M. MXene-based hybrid composites as photocatalyst for the mitigation of pharmaceuticals. *Chemosphere* **2021**, *291*, 133062. [\[CrossRef\]](#)
189. Sherryrna, A.; Tahir, M. Role of Ti_3C_2 MXene as prominent schottky barriers in driving hydrogen production through photoinduced water splitting: A comprehensive review. *ACS Appl. Energy Mater.* **2021**, *4*, 11982–12006. [\[CrossRef\]](#)
190. Sinopoli, A.; Othman, Z.; Rasool, K.; Mahmoud, K.A. Electrocatalytic/photocatalytic properties and aqueous media applications of 2D transition metal carbides (MXenes). *Curr. Opin. Solid State Mater. Sci.* **2019**, *23*, 100760. [\[CrossRef\]](#)
191. Huang, H.; Song, Y.; Li, N.; Chen, D.; Xu, Q.; Li, H.; He, J.; Lu, J. One-step in-situ preparation of N-doped $\text{TiO}_2@\text{C}$ derived from Ti_3C_2 MXene for enhanced visible-light driven photodegradation. *Appl. Catal. B Environ.* **2019**, *251*, 154–161. [\[CrossRef\]](#)
192. Wang, Y.; Yu, J.; Xiao, W.; Li, Q. Microwave-assisted hydrothermal synthesis of graphene based Au-TiO_2 photocatalysts for efficient visible-light hydrogen production. *J. Mater. Chem. A* **2014**, *2*, 3847–3855. [\[CrossRef\]](#)
193. Zhang, C.; Beidaghi, M.; Naguib, M.; Lukatskaya, M.R.; Zhao, M.-Q.; Dyatkin, B.; Cook, K.M.; Kim, S.J.; Eng, B.; Xiao, X. Synthesis and charge storage properties of hierarchical niobium pentoxide/carbon/niobium carbide (MXene) hybrid materials. *Chem. Mater.* **2016**, *28*, 3937–3943. [\[CrossRef\]](#)
194. Wang, H.; Wu, Y.; Xiao, T.; Yuan, X.; Zeng, G.; Tu, W.; Wu, S.; Lee, H.Y.; Tan, Y.Z.; Chew, J.W. Formation of quasi-core-shell $\text{In}_2\text{S}_3/\text{anatase TiO}_2$ on metallic $\text{Ti}_3\text{C}_2\text{Tx}$ hybrids with favorable charge transfer channels for excellent visible-light-photocatalytic performance. *Appl. Catal. B Environ.* **2018**, *233*, 213–225. [\[CrossRef\]](#)
195. Li, J.; Wang, S.; Du, Y.; Liao, W. Enhanced photocatalytic performance of $\text{TiO}_2@\text{C}$ nanosheets derived from two-dimensional Ti_2CT_x . *Ceram. Int.* **2018**, *44*, 7042–7046. [\[CrossRef\]](#)
196. Liu, M.; Qiu, X.; Miyauchi, M.; Hashimoto, K. Cu (II) oxide amorphous nanoclusters grafted Ti^{3+} self-doped TiO_2 : An efficient visible light photocatalyst. *Chem. Mater.* **2011**, *23*, 5282–5286. [\[CrossRef\]](#)
197. Mao, C.; Zuo, F.; Hou, Y.; Bu, X.; Feng, P. In situ preparation of a Ti^{3+} self-doped TiO_2 film with enhanced activity as photoanode by N_2H_4 reduction. *Angew. Chem.* **2014**, *126*, 10653–10657. [\[CrossRef\]](#)
198. Zhou, Y.; Liu, Y.; Liu, P.; Zhang, W.; Xing, M.; Zhang, J. A facile approach to further improve the substitution of nitrogen into reduced TiO_{2-x} with an enhanced photocatalytic activity. *Appl. Catal. B Environ.* **2015**, *170*, 66–73. [\[CrossRef\]](#)
199. Song, S.M.; Park, J.K.; Sul, O.J.; Cho, B.J. Determination of work function of graphene under a metal electrode and its role in contact resistance. *Nano Lett.* **2012**, *12*, 3887–3892. [\[CrossRef\]](#)
200. Zhao, L.; Dong, B.; Li, S.; Zhou, L.; Lai, L.; Wang, Z.; Zhao, S.; Han, M.; Gao, K.; Lu, M. Interdiffusion reaction-assisted hybridization of two-dimensional metal–organic frameworks and $\text{Ti}_3\text{C}_2\text{Tx}$ nanosheets for electrocatalytic oxygen evolution. *ACS Nano* **2017**, *11*, 5800–5807. [\[CrossRef\]](#) [\[PubMed\]](#)
201. Romero, E.; Novoderezhkin, V.I.; van Grondelle, R. Quantum design of photosynthesis for bio-inspired solar-energy conversion. *Nature* **2017**, *543*, 355–365. [\[CrossRef\]](#) [\[PubMed\]](#)
202. Long, M.; Brame, J.; Qin, F.; Bao, J.; Li, Q.; Alvarez, P.J. Phosphate changes effect of humic acids on TiO_2 photocatalysis: From inhibition to mitigation of electron–hole recombination. *Environ. Sci. Technol.* **2017**, *51*, 514–521. [\[CrossRef\]](#)

203. Iqbal, M.A.; Tariq, A.; Zaheer, A.; Gul, S.; Ali, S.I.; Iqbal, M.Z.; Akinwande, D.; Rizwan, S. Ti_3C_2 -MXene/bismuth ferrite nanohybrids for efficient degradation of organic dyes and colorless pollutants. *ACS Omega* **2019**, *4*, 20530–20539. [[CrossRef](#)] [[PubMed](#)]
204. Fang, Y.; Cao, Y.; Chen, Q. Synthesis of an $\text{Ag}_2\text{WO}_4/\text{Ti}_3\text{C}_2$ Schottky composite by electrostatic traction and its photocatalytic activity. *Ceram. Int.* **2019**, *45*, 22298–22307. [[CrossRef](#)]
205. Zhang, G.; Wu, S.; Li, Y.; Zhang, Q. Significant improvement in activity, durability, and light-to-fuel efficiency of Ni nanoparticles by La_2O_3 cluster modification for photothermocatalytic CO_2 reduction. *Appl. Catal. B Environ.* **2020**, *264*, 118544. [[CrossRef](#)]
206. Ghobadifard, M.; Mohebbi, S. Novel nanomagnetic $\text{Ag}/\beta\text{-Ag}_2\text{WO}_4/\text{CoFe}_2\text{O}_4$ as a highly efficient photocatalyst under visible light irradiation. *New J. Chem.* **2018**, *42*, 9530–9542. [[CrossRef](#)]
207. Zou, Y.; Shi, J.-W.; Sun, L.; Ma, D.; Mao, S.; Lv, Y.; Cheng, Y. Energy-band-controlled $\text{Zn}_x\text{Cd}_{1-x}\text{In}_2\text{S}_4$ solid solution coupled with g- C_3N_4 nanosheets as 2D/2D heterostructure toward efficient photocatalytic H_2 evolution. *Chem. Eng. J.* **2019**, *378*, 122192. [[CrossRef](#)]
208. Yuan, X.; Jiang, L.; Liang, J.; Pan, Y.; Zhang, J.; Wang, H.; Leng, L.; Wu, Z.; Guan, R.; Zeng, G. In-situ synthesis of 3D microsphere-like $\text{In}_2\text{S}_3/\text{InVO}_4$ heterojunction with efficient photocatalytic activity for tetracycline degradation under visible light irradiation. *Chem. Eng. J.* **2019**, *356*, 371–381. [[CrossRef](#)]
209. Mi, Y.; Wen, L.; Wang, Z.; Cao, D.; Fang, Y.; Lei, Y. Building of anti-restack 3D BiOCl hierarchy by ultrathin nanosheets towards enhanced photocatalytic activity. *Appl. Catal. B Environ.* **2015**, *176*, 331–337. [[CrossRef](#)]
210. Shi, X.; Wang, P.; Lan, L.; Jia, S.; Wei, Z. Construction of $\text{BiOBr}/\text{I}_1-x/\text{MXene } \text{Ti}_3\text{C}_2\text{Tx}$ composite for improved photocatalytic degradability. *J. Mater. Sci. Mater. Electron.* **2019**, *30*, 19804–19812. [[CrossRef](#)]
211. Tariq, A.; Ali, S.I.; Akinwande, D.; Rizwan, S. Efficient visible-light photocatalysis of 2D-MXene nanohybrids with Gd^{3+} - and Sn^{4+} -codoped bismuth ferrite. *ACS Omega* **2018**, *3*, 13828–13836. [[CrossRef](#)]
212. Ran, J.; Gao, G.; Li, F.-T.; Ma, T.-Y.; Du, A.; Qiao, S.-Z. Ti_3C_2 MXene co-catalyst on metal sulfide photo-absorbers for enhanced visible-light photocatalytic hydrogen production. *Nat. Commun.* **2017**, *8*, 13907. [[CrossRef](#)] [[PubMed](#)]
213. Persson, I.; Näslund, L.-Å.; Halim, J.; Barsoum, M.W.; Darakchieva, V.; Palisaitis, J.; Rosen, J.; Persson, P.O.Å. On the organization and thermal behavior of functional groups on Ti_3C_2 MXene surfaces in vacuum. *2D Mater.* **2017**, *5*, 015002. [[CrossRef](#)]
214. Pandey, R.P.; Rasheed, P.A.; Gomez, T.; Azam, R.S.; Mahmoud, K.A. A fouling-resistant mixed-matrix nanofiltration membrane based on covalently cross-linked $\text{Ti}_3\text{C}_2\text{Tx}$ (MXene)/cellulose acetate. *J. Membr. Sci.* **2020**, *607*, 118139. [[CrossRef](#)]
215. Alessandro, F.; Macedonio, F.; Drioli, E. New Materials and Phenomena in Membrane Distillation. *Chemistry* **2023**, *5*, 65–84. [[CrossRef](#)]
216. Gugliuzza, A.; Macedonio, F.; Politano, A.; Drioli, E. Prospects of 2D materials-based membranes in water desalination. *Chem. Eng. Trans* **2019**, *73*, 265–270.
217. Kang, K.M.; Kim, D.W.; Ren, C.E.; Cho, K.M.; Kim, S.J.; Choi, J.H.; Nam, Y.T.; Gogotsi, Y.; Jung, H.-T. Selective molecular separation on $\text{Ti}_3\text{C}_2\text{Tx}$ -graphene oxide membranes during pressure-driven Filtration: Comparison with graphene oxide and MXenes. *ACS Appl. Mater. Interfaces* **2017**, *9*, 44687–44694. [[CrossRef](#)]
218. Ding, L.; Wei, Y.; Wang, Y.; Chen, H.; Caro, J.; Wang, H. A two-dimensional lamellar membrane: MXene nanosheet stacks. *Angew. Chem. Int. Ed.* **2017**, *56*, 1825–1829. [[CrossRef](#)]
219. Pandey, R.P.; Rasool, K.; Madhavan, V.E.; Aïssa, B.; Gogotsi, Y.; Mahmoud, K.A. Ultrahigh-flux and fouling-resistant membranes based on layered silver/MXene ($\text{Ti}_3\text{C}_2\text{Tx}$) nanosheets. *J. Mater. Chem. A* **2018**, *6*, 3522–3533. [[CrossRef](#)]
220. Ding, L.; Li, L.; Liu, Y.; Wu, Y.; Lu, Z.; Deng, J.; Wei, Y.; Caro, J.; Wang, H. Effective ion sieving with $\text{Ti}_3\text{C}_2\text{Tx}$ MXene membranes for production of drinking water from seawater. *Nat. Sustain.* **2020**, *3*, 296–302. [[CrossRef](#)]
221. Lu, Z.; Wei, Y.; Deng, J.; Ding, L.; Li, Z.-K.; Wang, H. Self-crosslinked MXene ($\text{Ti}_3\text{C}_2\text{Tx}$) membranes with good anti-swelling property for monovalent metal ion exclusion. *ACS Nano* **2019**, *13*, 10535–10544. [[CrossRef](#)]
222. Sun, Y.; Li, S.; Zhuang, Y.; Liu, G.; Xing, W.; Jing, W. Adjustable interlayer spacing of ultrathin MXene-derived membranes for ion rejection. *J. Membr. Sci.* **2019**, *591*, 117350. [[CrossRef](#)]
223. Wang, J.; Zhang, Z.; Zhu, J.; Tian, M.; Zheng, S.; Wang, F.; Wang, X.; Wang, L. Ion sieving by a two-dimensional $\text{Ti}_3\text{C}_2\text{Tx}$ alginate lamellar membrane with stable interlayer spacing. *Nat. Commun.* **2020**, *11*, 3540. [[CrossRef](#)]
224. Sun, Y.; Xu, D.; Li, S.; Cui, L.; Zhuang, Y.; Xing, W.; Jing, W. Assembly of multidimensional MXene-carbon nanotube ultrathin membranes with an enhanced anti-swelling property for water purification. *J. Membr. Sci.* **2021**, *623*, 119075. [[CrossRef](#)]
225. Yaroshchuk, A.; Bruening, M.L.; Bernal, E.E.L. Solution-Diffusion-Electro-Migration model and its uses for analysis of nanofiltration, pressure-retarded osmosis and forward osmosis in multi-ionic solutions. *J. Membr. Sci.* **2013**, *447*, 463–476. [[CrossRef](#)]
226. Li, K.; Tao, Y.; Li, Z.; Sha, J.; Chen, Y. Selective ion-permeation through strained and charged graphene membranes. *Nanotechnology* **2017**, *29*, 035402. [[CrossRef](#)]
227. Wu, X.; Ding, M.; Xu, H.; Yang, W.; Zhang, K.; Tian, H.; Wang, H.; Xie, Z. Scalable $\text{Ti}_3\text{C}_2\text{Tx}$ mxene interlayered forward osmosis membranes for enhanced water purification and organic solvent recovery. *ACS Nano* **2020**, *14*, 9125–9135. [[CrossRef](#)]
228. Wang, X.; Li, Q.; Zhang, J.; Huang, H.; Wu, S.; Yang, Y. Novel thin-film reverse osmosis membrane with MXene $\text{Ti}_3\text{C}_2\text{Tx}$ embedded in polyamide to enhance the water flux, anti-fouling and chlorine resistance for water desalination. *J. Membr. Sci.* **2020**, *603*, 118036. [[CrossRef](#)]
229. Meng, B.; Liu, G.; Mao, Y.; Liang, F.; Liu, G.; Jin, W. Fabrication of surface-charged MXene membrane and its application for water desalination. *J. Membr. Sci.* **2021**, *623*, 119076. [[CrossRef](#)]

230. Fuzil, N.S.; Othman, N.H.; Alias, N.H.; Marpani, F.; Othman, M.H.D.; Ismail, A.F.; Lau, W.J.; Li, K.; Kusworo, T.D.; Ichinose, I. A review on photothermal material and its usage in the development of photothermal membrane for sustainable clean water production. *Desalination* **2021**, *517*, 115259. [\[CrossRef\]](#)
231. Liu, Y.; Zhao, J.; Zhang, S.; Li, D.; Zhang, X.; Zhao, Q.; Xing, B. Advances and challenges of broadband solar absorbers for efficient solar steam generation. *Environ. Sci. Nano* **2022**, *9*, 2264–2296. [\[CrossRef\]](#)
232. Huang, L.; Pei, J.; Jiang, H.; Hu, X. Water desalination under one sun using graphene-based material modified PTFE membrane. *Desalination* **2018**, *442*, 1–7. [\[CrossRef\]](#)
233. Li, Z.; Lei, H.; Kan, A.; Xie, H.; Yu, W. Photothermal applications based on graphene and its derivatives: A state-of-the-art review. *Energy* **2021**, *216*, 119262. [\[CrossRef\]](#)
234. Li, W.; Chen, Y.; Yao, L.; Ren, X.; Li, Y.; Deng, L. Fe₃O₄/PVDF-HFP photothermal membrane with in-situ heating for sustainable, stable and efficient pilot-scale solar-driven membrane distillation. *Desalination* **2020**, *478*, 114288. [\[CrossRef\]](#)
235. Wu, X.; Jiang, Q.; Ghim, D.; Singamaneni, S.; Jun, Y.-S. Localized heating with a photothermal polydopamine coating facilitates a novel membrane distillation process. *J. Mater. Chem. A* **2018**, *6*, 18799–18807. [\[CrossRef\]](#)
236. Politano, A.; Di Profio, G.; Fontananova, E.; Sanna, V.; Cupolillo, A.; Curcio, E. Overcoming temperature polarization in membrane distillation by thermoplasmonic effects activated by Ag nanofillers in polymeric membranes. *Desalination* **2019**, *451*, 192–199. [\[CrossRef\]](#)
237. Li, H.; He, Y.; Liu, Z.; Jiang, B.; Huang, Y. A flexible thin-film membrane with broadband Ag@TiO₂ nanoparticle for high-efficiency solar evaporation enhancement. *Energy* **2017**, *139*, 210–219. [\[CrossRef\]](#)
238. Xu, D.; Li, Z.; Li, L.; Wang, J. Insights into the photothermal conversion of 2D MXene nanomaterials: Synthesis, mechanism, and applications. *Adv. Funct. Mater.* **2020**, *30*, 2000712. [\[CrossRef\]](#)
239. Dongare, P.D.; Alabastri, A.; Pedersen, S.; Zodrow, K.R.; Hogan, N.J.; Neumann, O.; Wu, J.; Wang, T.; Deshmukh, A.; Elimelech, M. Nanophotonics-enabled solar membrane distillation for off-grid water purification. *Proc. Natl. Acad. Sci. USA* **2017**, *114*, 6936–6941. [\[CrossRef\]](#)
240. Bamasag, A.; Almatrafi, E.; Alqahtani, T.; Phelan, P.; Ullah, M.; Mustakeem, M.; Obaid, M.; Ghaffour, N. Recent advances and future prospects in direct solar desalination systems using membrane distillation technology. *J. Clean. Prod.* **2022**, *385*, 135737. [\[CrossRef\]](#)
241. Cao, S.; Wu, X.; Zhu, Y.; Gupta, P.; Martinez, A.; Zhang, Y.; Ghim, D.; Wang, Y.; Liu, L.; Jun, Y.-S. MXene aerogel for efficient photothermally driven membrane distillation with dual-mode antimicrobial capability. *J. Mater. Chem. A* **2021**, *9*, 22585–22596. [\[CrossRef\]](#)
242. Tan, Y.Z.; Wang, H.; Han, L.; Tanis-Kanbur, M.B.; Pranav, M.V.; Chew, J.W. Photothermal-enhanced and fouling-resistant membrane for solar-assisted membrane distillation. *J. Membr. Sci.* **2018**, *565*, 254–265. [\[CrossRef\]](#)
243. Chen, L.; Shi, X.; Yu, N.; Zhang, X.; Du, X.; Lin, J. Measurement and analysis of thermal conductivity of Ti₃C₂T_x MXene films. *Materials* **2018**, *11*, 1701. [\[CrossRef\]](#) [\[PubMed\]](#)
244. Gholivand, H.; Fuladi, S.; Hemmat, Z.; Salehi-Khojin, A.; Khalili-Araghi, F. Effect of surface termination on the lattice thermal conductivity of monolayer Ti₃C₂Tz MXenes. *J. Appl. Phys.* **2019**, *126*, 065101. [\[CrossRef\]](#)
245. Jiang, X.; Kuklin, A.V.; Baev, A.; Ge, Y.; Ågren, H.; Zhang, H.; Prasad, P.N. Two-dimensional MXenes: From morphological to optical, electric, and magnetic properties and applications. *Phys. Rep.* **2020**, *848*, 1–58. [\[CrossRef\]](#)
246. Khan, R.; Andreescu, S. Mxenes-based bioanalytical sensors: Design, characterization, and applications. *Sensors* **2020**, *20*, 5434. [\[CrossRef\]](#)
247. Dong, L.M.; Ye, C.; Zheng, L.L.; Gao, Z.F.; Xia, F. Two-dimensional metal carbides and nitrides (MXenes): Preparation, property, and applications in cancer therapy. *Nanophotonics* **2020**, *9*, 2125–2145. [\[CrossRef\]](#)
248. Peng, Y.-Y.; Akuzum, B.; Kurra, N.; Zhao, M.-Q.; Alhabeab, M.; Anasori, B.; Kumbur, E.C.; Alshareef, H.N.; Ger, M.-D.; Gogotsi, Y. All-MXene (2D titanium carbide) solid-state microsupercapacitors for on-chip energy storage. *Energy Environ. Sci.* **2016**, *9*, 2847–2854. [\[CrossRef\]](#)
249. Zhang, J.; Seyedin, S.; Gu, Z.; Yang, W.; Wang, X.; Razal, J.M. MXene: A potential candidate for yarn supercapacitors. *Nanoscale* **2017**, *9*, 18604–18608. [\[CrossRef\]](#)
250. Zhang, J.; Wan, L.; Gao, Y.; Fang, X.; Lu, T.; Pan, L.; Xuan, F. Highly stretchable and self-healable MXene/polyvinyl alcohol hydrogel electrode for wearable capacitive electronic skin. *Adv. Electron. Mater.* **2019**, *5*, 1900285. [\[CrossRef\]](#)
251. Liu, R.; Li, W. High-thermal-stability and high-thermal-conductivity Ti₃C₂T_x MXene/poly (vinyl alcohol)(PVA) composites. *ACS Omega* **2018**, *3*, 2609–2617. [\[CrossRef\]](#) [\[PubMed\]](#)
252. Kim, H.; Alshareef, H.N. MXetronics: MXene-enabled electronic and photonic devices. *ACS Mater. Lett.* **2019**, *2*, 55–70. [\[CrossRef\]](#)
253. Li, J.; Yan, D.; Hou, S.; Li, Y.; Lu, T.; Yao, Y.; Pan, L. Improved sodium-ion storage performance of Ti₃C₂T_x MXenes by sulfur doping. *J. Mater. Chem. A* **2018**, *6*, 1234–1243. [\[CrossRef\]](#)
254. Liu, B.; Pouramini, S. Multi-objective optimization for thermal comfort enhancement and greenhouse gas emission reduction in residential buildings applying retrofitting measures by an Enhanced Water Strider Optimization Algorithm: A case study. *Energy Rep.* **2021**, *7*, 1915–1929. [\[CrossRef\]](#)
255. Nasrallah, G.K.; Al-Asmakh, M.; Rasool, K.; Mahmoud, K.A. Ecotoxicological assessment of Ti₃C₂T_x (MXene) using a zebrafish embryo model. *Environ. Sci. Nano* **2018**, *5*, 1002–1011. [\[CrossRef\]](#)

256. Jastrzębska, A.; Szuplewska, A.; Wojciechowski, T.; Chudy, M.; Ziemkowska, W.; Chlubny, L.; Rozmysłowska, A.; Olszyna, A. In vitro studies on cytotoxicity of delaminated Ti_3C_2 MXene. *J. Hazard. Mater.* **2017**, *339*, 1–8. [[CrossRef](#)]
257. Alhussain, H.; Augustine, R.; Hussein, E.A.; Gupta, I.; Hasan, A.; Al Moustafa, A.-E.; Elzatahry, A. MXene nanosheets may induce toxic effect on the early stage of embryogenesis. *J. Biomed. Nanotechnol.* **2020**, *16*, 364–372. [[CrossRef](#)]

Disclaimer/Publisher’s Note: The statements, opinions and data contained in all publications are solely those of the individual author(s) and contributor(s) and not of MDPI and/or the editor(s). MDPI and/or the editor(s) disclaim responsibility for any injury to people or property resulting from any ideas, methods, instructions or products referred to in the content.